ACCEPTED VERSION

http://hdl.handle.net/2440/81130

Keywords: Cambrian; carbonate; thrombolite; skeletons; archaeocyath

GEOBIOLOGY OF A LOWER CAMBRIAN CARBONATE PLATFORM, PEDROCHE FORMATION, OSSA MORENA ZONE, SPAIN

Jessica R. Creveling[a*1], David Fernández Remolar[b], Marta Rodríguez-Martínez[c], Silvia Menéndez[d], Kristin D. Bergmann[e], Benjamin C. Gill[f], John Abelson[g], Ricardo Amils[b,h], Bethany L. Ehlmann[e], Diego C. García-Bellido[i], John P. Grotzinger[e], Christian Hallmann[j,k],

Kathryn M. Stack[e], Andrew H. Knoll[a,l]

[a]*Department of Earth and Planetary Sciences, Harvard University, Cambridge, MA, U.S.A., 02138*

[b]*Centro de Astrobiología, Instituto Nacional de Técnica Aeroespaciales, 28850 Torrejón de Ardoz, Spain*

[c]*Departamento de Estratigrafía, Facultad de Ciencias Geológicas, Universidad Complutense de Madrid, 28041 Madrid, Spain*

[d]*Museo Geominero, Instituto Geológico y Minero, 28003 Madrid, Spain*

[e]*Division of Geological and Planetary Sciences, California Institute of Technology, CA, U.S.A., 91125*

[f]*Department of Geosciences, Virginia Polytechnic Institute and State University, Blacksburg, VA, U.S.A. 24061*

[g]*The Agouron Institute, Pasadena, CA, U.S.A., 91106*

[h]*Centro de Biología Molecular Severo Ochoa, Universidad Autónoma de Madrid, 28048 Madrid, Spain*

[i]*Instituto de Geociencias (CSIC, UCM), José Antonio Novais 2, 20816 Madrid, Spain*

[j]*Max-Planck-Institute for Biogeochemistry, 07745 Jena, Germany*

[k]*MARUM, Universität Bremen, 28359 Bremen, Germany*

[l]*Department of Organismic and Evolutionary Biology, Harvard University, Cambridge, MA, U.S.A., 02138*

*Corresponding author. E-mail address: jcrevel@gps.caltech.edu (J.R. Creveling). Tel.: +1 626 395 1783.
[1]*Present address: California Institute of Technology, Division of Geological and Planetary Sciences, MC 100-23, 1200 E. California Blvd., Pasadena, CA, 91125, U.S.A.*

ABSTRACT

The Cambrian Pedroche Formation comprises a mixed siliciclastic–carbonate succession recording subtidal deposition on a marine platform. Carbonate carbon isotope chemostratigraphy confirms previous biostratigraphic assignment of the Pedroche Formation to the Atdabanian regional stage of Siberia, correlative to Cambrian Series 2. At the outcrop scale, thrombolitic facies comprise ~60% of carbonate-normalized stratigraphy and coated-grains another ~10%. Petrographic point counts reveal that skeletons contribute at most 20% to thrombolitic inter-reef and reef-flank lithologies; on average, archaeocyath clasts make up 68% of skeletal materials. In contrast, petrographic point counts show that skeletons comprise a negligible volume of both the biohermal and biostromal thrombolite and associated nodular carbonate facies, as well as the ooid, oncoid, and peloid grainstone facies. As such, archaeocyathan reefal bioconstructions represent a specific and limited locus of skeletal carbonate production and deposition. Consistent with data from coeval, globally dispersed lower Cambrian successions, our analysis of the Pedroche Formation supports the view that early Cambrian carbonates have more in common with earlier, Neoproterozoic deposits than with younger carbonates dominated by skeletal production and accumulation.

1. INTRODUCTION

Today, skeletons account for most carbonate accumulation in the oceans (e.g., Sarmiento and Gruber, 2006). The geological record, however, shows that this was not the case for most of Earth history; Archean and Proterozoic successions contain thick packages of shallow-marine carbonates deposited via abiotic and microbially-mediated precipitation (e.g., Grotzinger, 1989; Knoll and Swett, 1990; Grotzinger and James, 2000). With this in mind, a canonical view holds that the Cambrian diversification of skeletal animals (Maloof et al., 2010a; Kouchinsky et al., 2012) was a watershed event in the evolution of platform and shelf carbonate deposition (e.g., Zeebe and Westbroek, 2003). Yet, the idea that the nature of carbonate production irrevocably changed with the advent of skeletal biomineralization is hard to reconcile with uppermost Neoproterozoic and Cambrian carbonates whose textures resemble Proterozoic platform archetypes despite a quantifiable skeletal contribution.

Where, then, do Cambrian shelf and platform carbonates fall along the spectrum of non-skeletal to skeletal control? Might the Cambrian Period represent a time when organisms had evolved biomineralized skeletons but not yet transformed ecosystem ecology? Analysis of upper Cambrian and lower Ordovician carbonates from Laurentia provides support for this view; in successions from Newfoundland and the North American Cordillera, skeletal material rarely exceeds 25% of bulk carbonate volume and is commonly much less (Pruss et al., 2010). Upper Cambrian rocks, however, might understate the case for skeletal input to Cambrian carbonates, in large part because archaeocyaths, the most conspicuous Cambrian reef-constructing animals, had nearly disappeared by 510 Ma (Debrenne, 2007). Preliminary research on earlier Cambrian carbonates suggests that skeletons contributed up to ~ 20% of total carbonate production, with archaeocyathan material dominating skeletal input (Hicks and Rowland, 2009; Pruss et al., 2012).

Here we provide a new case study of carbonate production on an early Cambrian carbonate platform that hosted thrombolite archaeocyath-bearing reefs. We focus on the nature of carbonate production and the percent skeletal abundance within three stratigraphic sections of the Cambrian Series 2 Pedroche Formation, Córdoba, southern Spain. We build from the sedimentological and biostratigraphic framework developed for the Pedroche Formation by numerous authors. The Pedroche Formation at the Arroyo Pedroche section has been analyzed and discussed previously by Carbonell (1926, 1929, 1930a-g), Cabanás and Meléndez (1966), Perejón (1975 a, b, c; 1976a,b; 1977, 1986, 1989), Cabanás (1971), Liñán (1974, 1978), Liñán and Dabrio (1974), Liñán et al. (1981), Liñán and Mergl (1982), Schmitt (1982), Moreno-Eiris (1987 a, b, c, d), Moreno-Eiris et al. (1995), and Fernández-Remolar (1996, 1998). The Pedroche Formation at the Cerro de Las Ermitas section has been studied previously by Hernández Pacheco (1907; 1917; 1918a, b; 1926), Hernández-Sampelayo (1933, 1935), Simon (1939), Perejón (1976a,b; 1971; 1975 a, b, c; 1986), Cabanás (1971), Zamarreño and Debrenne (1977), Moreno-Eiris (1987 a, b, c, d), Fernández-Remolar (1996, 1998, 1999, 2001, 2002), and Perejón and Moreno-Eiris (2007). Finally, Zamarreño (1977) studied the Pedroche Formation at the Pilgrimage Road section.

To complement and extend this body of research, we use $\delta^{13}C_{carb}$ chemostratigraphy to establish local and global temporal correlations. Next, we analyze the architecture of thrombolite and associated carbonate facies from this mixed carbonate-siliciclastic platform developed on a peri-Gondwana terrane during the early Cambrian. To do so, we follow the methodology of Pruss et al. (2010) and use nested scale observations, from outcrop stratigraphy to petrographic analysis of carbonate facies, to quantify the contribution of skeletal material to carbonate

lithofacies and assess the nature of carbonate production across the platform. Finally, we compare these findings with other early Cambrian localities with quantitative lithologic and skeletal composition data.

2. GEOLOGIC SETTING

The three outcrops of the Pedroche Formation studied here occur within the Sierra de Córdoba, near the city of Córdoba, within the Ossa-Morena tectonostratigraphic zone of the Iberian Massif (Lotze, 1945; Julivert et al., 1972; Dallmeyer and Martínez García, 1990; Ábalos et al., 2002; Pérez-Estaún and Bea, 2004). The Ossa-Morena zone records a complex history of Neoproterozoic and Paleozoic extension, sedimentation and orogenesis resulting from the geodynamic interactions among Gondwana, Laurentia, Baltica, and proximal micro-continents, including Iberia (see, for example, Eguíluz et al., 2000; Dallmeyer and Martínez García, 1990). Broadly, the tectonostratigraphy of the Ossa-Morena zone documents Neoproterozoic Cadomian and middle-to-late Paleozoic Hercynian orogenisis, each followed by sedimentation during rift-to-drift (passive margin) transition (Eguíluz et al., 2000). These Neoproterozoic to Paleozoic strata were uplifted in the southwest European Variscan Orogen as a result of the collision between Laurentia and Gondwana during the Devonian to Permian Periods (Bard et al., 1980; Matte, 1991).

Liñán (1974, 1978) developed the Cambrian sequence stratigraphic framework for the Sierra de Córdoba region (summarized in Figure 1a). Cambrian strata unconformably overlie the San Jerónimo Formation of the Neoproterozoic volcanic-sedimentary complex (Liñán and Palacios, 1983; Fedonkin et al., 1983). From oldest to youngest, the Cambrian stratigraphy is divided into the following formations (see the overview in Gozalo et al., 2003): (i) the siliciclastic-dominated Torreárboles Formation (0-300 m), assigned to the Spanish Corduban stage based on its trace fossil assemblage (Fedonkin et al., 1983); (ii) the mixed carbonate-siliciclastic Pedroche Formation (350 m), which represents the Ovetian stage (detailed biostratigraphic references discussed below); (iii) the mixed carbonate and siliciclastic Santo Domingo Formation (200 m) representing the Marianian stage; (iv) the Castellar Formation (~75 m), assigned to the Bilbilian based on stratigraphic position (Liñán et al., 1997); and (v) the siliciclastic Los Villares Formation (> 450 m) ranging from Bilbilian to middle Cambrian in age (Liñán and Sdzuy, 1978; Liñán 1978). Here we focus on fossiliferous carbonates of the Pedroche Formation.

The Pedroche Formation records the first stable carbonate platform development after Cadomian rifting (Liñán and Quesada, 1990; Quesada, 1990; Menéndez et al., 1999). Trilobite (Liñán et al., 2005; Liñán et al., 2008), archaeocyath (Perejón, 1986; 1989; 1994) and small shelly fossil (Fernández-Remolar, 2001; Gubanov et al., 2004; Hinz-Schallreuter et al., 2008) biostratigraphy assign the Pedroche to the early Ovetian Stage of the Iberian chronostratigraphic framework (Liñán et al., 1993 and references therein). Archaeocyathan taxa of the Pedroche Formation correlate to Spanish archaeocyathan Zones I – III , correlative to the Atdabanian 1-2 stage of Siberia (Perejón and Moreno-Eiris, 2006). The occurrence of the bigotinid trilobites *Bigotina* and *Lemdadella* within these zones also supports an early Atdabanian age (Liñán and Gámez Vintanez, 1993; Liñán et al., 1995, 2005, 2008). As such, the Pedroche Formation records deposition correlative to Cambrian Series 2, Stage 3 of the international chronostratigraphy for the Cambrian System (Fig. 1a; Jensen et al., 2010; Babcock and Peng, 2007; Peng and Babcock, 2011).

3. METHODS

Stratigraphic sections of the Pedroche Formation were described and measured at three localities in the vicinity of Córdoba, Andalucía, Spain (Fig. 1b). The type section for the formation, Arroyo Pedroche (Section AP; 37°54'26.67"N, 4°45'29.07"W), crops out along the east embankment of an arroyo. Additionally, the Pedroche Formation is exposed north-northeast of the city, within the Sierra de Córdoba, where strata crop out along the north side of a hairpin turn on CO-110, herein referred to as Pilgrimage Road (Section PR; 37°55'45"N, 4°49'02"W), as well as on the east side of road CV-079 leading to Cerro de Las Ermitas (Section LE; 37°55'05.25"N, 4°49'34.66"W), just above the fifth station of the cross.

We determined the percent contribution of carbonate lithofacies to each stratigraphic section by adding up the bed thicknesses of a lithofacies (e.g., ooid/oncoid/peloid grainstone), dividing this value by the total meterage from each section, and multiplying this decimal by 100 (Table 1). Likewise, we determined the 'carbonate-normalized' percent contribution of a carbonate lithofacies to a stratigraphic section through the method described above, except in this case we divide by the total *carbonate* meterage of the section. Within the lithofacies descriptions we use the terminology of Ingram (1954) to describe laminae and bed thickness (thinly laminated: < 3mm; thickly laminated: 3-10 mm; very thinly bedded: 1-3 cm; thinly bedded: 3-10 cm; medium bedded: 10-30 cm; thickly bedded: 30-100 cm; and very thickly bedded: > 1m). However, our field descriptions include cm-scale measurements of each bed in order to best estimate the percent contribution of each lithofacies to the three stratigraphic sections measured.

We collected hand samples of carbonate lithofacies at ~1 to 2 meter resolution. The samples were cut with a water-cooled saw perpendicular to bedding to create slabs and thin-section billets. Each slab or billet was micro-drilled with a 1 mm dental bit for carbonate carbon ($\delta^{13}C_{carb}$) and carbonate oxygen ($\delta^{18}O_{carb}$) isotopic analysis. We targeted micritic textures and avoided veins, cements and skeletal elements. Carbonate powder was reacted in a common phosphoric acid bath at 90°C for 7 minutes. Evolved CO_2 was cryogenically concentrated and measured against an in-house reference gas on a VG Optima dual-inlet mass spectrometer attached to a VG Isocarb preparation system. All isotopic values are reported in per mil (‰) notation relative to the V-PDB standard with a reproducibility of $1\sigma \approx 0.1‰$ and $0.3‰$ for $\delta^{13}C_{carb}$ and $\delta^{18}O_{carb}$, respectively.

Point-counts of petrographic thin-sections enabled us to quantify the proportional contributions of constituent components to carbonate volume (e.g., Flügel, 2004; Payne et al., 2006; Pruss et al., 2010; Pruss and Clemente, 2011). Of the 74 thin-sections examined for lithofacies description, we point counted 30 thin sections for quantitative analysis of constituent components, with 5 representing the calcimicrobial thrombolite facies (facies A), 9 representing the ooid/oncoid/peloid grainstone facies (facies C), and 16 representing the interbedded carbonate mudstone, bioclastic wackestone, archaeocyathan floatstone–packstone–rudstone and siliciclastic siltstone facies assemblage (facies D; see text for lithofacies description; Table 2). We chose these thin sections because they exhibit the least secondary recrystallization (spar and veins) of all the hand samples collected while measuring stratigraphic sections.

The statistical robustness of point count frequency analyses depends on the density of the point array (grid spacing) with respect to the size and percent contribution of individual components (Van der Plas and Tobi, 1965; Flügel, 2004). Generally, the width of the chosen grid-spacing relative to the largest diameter of the constituent components (e.g., micrite, ooids or archaeocyaths) dictates whether the counting procedure over-represents coarse grains (dense

grid) or under-represents fine grains (sparse grid) (Van der Plas and Tobi, 1965; Flügel, 2004). We used transmitted light microscopy to classify ~200 points per thin-section, corresponding to a 2 x 2 mm width grid spacing. This point-density translates to 2σ errors of ~2, 4, and 5.5% for constituent components calculated to comprise ~3, 9, and 20% of the sample, respectively. In other words, a sample determined to have 9% skeletal content by point-count analysis should be considered to have 9 ± 4% with 95% confidence (Van der Plas and Tobi, 1965; Flügel, 2004).

Lithologies and microtextures of the Pedroche Formation, particularly the archaeocyath-bearing facies, consist of submicron- to centimeter-scale crystals and grains. As such, the use of a fixed grid spacing introduces a potential bias towards grains larger than 2 x 2 mm width / circumference. We note, however, that the true skeletal component of large skeletal grains, such as archaeocyaths, comprise only a fraction of the total encompassing volume. For this reason, we employ the grain-solid method of point counting wherein only the solid fraction of a skeleton is classified as skeletal contribution; any primary inter-skeletal void space, such as the central cavity of an archaeocyath, is counted separately under relevant textural classifications, such as micrite or sparry cement (Flügel, 2004). As such, we believe the chosen grid spacing should not over represent the largest diameter constituents. We adopted this method from Pruss et al. (2012) so that we could directly compare the percentage of constituent carbonate fabrics and, in particular, the skeletal content of the Pedroche Formation to archaeocyath-bearing Cambrian Series 2 reefs from the Forteau Formation, southern Labrador.

A subset of the thin-sections analyzed had surface areas too small to count 200 points per slide at 2 mm spacing. Instead of increasing the point density (decreasing the grid spacing) counted on these slides—which would have shifted the bias in grain size relative to the 2 mm grid—we report fewer than 200 points for these samples with the caveat that larger 2σ uncertainties in the percent determinations of constituent components are associated with these samples. Nevertheless, for this subset of samples we counted between 164 and 198 points, therefore the additional uncertainly incurred from these lower point counts should not significantly influence the conclusions of this study.

4. CARBON ISOTOPIC CHEMOSTRATIGRAPHY

Figure 2 presents a 3-point moving average of carbonate carbon isotope ($\delta^{13}C_{carb}$) chemostratigraphy for the AP and PR sections, and un-averaged data for the LE section. (See Supplementary Information for a table of raw $\delta^{13}C_{carb}$ and $\delta^{18}O_{carb}$ values, covariance plots of $\delta^{13}C_{carb}$ versus $\delta^{18}O_{carb}$, and chemostratigraphic plots of both un-averaged and 3-point running means of $\delta^{13}C_{carb}$ for all three stratigraphic sections.) Arroyo Pedroche $\delta^{13}C_{carb}$ values display a positive trend from 1.9 to 3.3‰ from 32–37 m that precedes a negative excursion to a nadir of -1.3‰ at 67 m. Above the covered interval from ~68.1–81 m, $\delta^{13}C_{carb}$ values resume at -2.0‰, plateau at ~ -1.4‰ between 82.9–119.1 m, and increase to -0.5‰ by 129 m. At the Pilgrimage Road section, $\delta^{13}C_{carb}$ values show a broadly similar pattern of stratigraphic variation, increasing from -1.8 to 1.0‰ from the base of the section to 30.5 m, declining to a nadir of -2.9‰ at 52 m, and then rebounding toward broadly stable values of -1 to -2 in the upper part of the section (except for a transient negative excursion to -2.9‰ at 89 m). The carbon isotope composition of carbonates of the Las Ermitas section remains invariant at ~ -1.5‰.

Correlation between $\delta^{13}C_{carb}$ and $\delta^{18}O_{carb}$ values in samples from the Arroyo Pedroche section 0–63 m and Las Ermitas section 0–13 m is best explained by a linear regression model ($R^2 = 0.71$ for both sections). Conversely, no linear covariance between $\delta^{13}C_{carb}$ and $\delta^{18}O_{carb}$

values is observed in these two sections above these stratigraphic intervals ($R^2 = 0.15$ and 0.35, respectively), nor is covariance observed within the Pilgrimage Road section ($R^2 = 0.14$). Covariance between $\delta^{13}C_{carb}$ and $\delta^{18}O_{carb}$ values, as well as isotopically depleted $\delta^{18}O_{carb}$ values, provides strong evidence for diagenetic overprint of primary seawater isotopic compositions (e.g., Knauth and Kennedy, 2009; Derry, 2010 and references therein). While petrography indicates significant neomorphism of these limestones (see detailed discussion below), we note that carbonate petrographic textures do not differ between intervals with and without $\delta^{13}C_{carb}$–$\delta^{18}O_{carb}$ covariation.

An alternative way to address the possibility of whole rock diagenesis is to ask how well the chemostratigraphic variation within the Pedroche Formation correlates to chemostratigraphic variability from biostratigraphically equivalent time periods elsewhere around the globe. The well-constrained biostratigraphic assignment of Pedroche carbonates to the early Ovetian, equivalent to the base of Cambrian Series 2 and the Siberian Atdabanian Stage (Jensen et al., 2010) makes a prediction for their C-isotopic composition. Consistent with this prediction, $\delta^{13}C_{carb}$ values from Arroyo Pedroche appear to capture the apex of a positive excursion, with absolute values like those of the early Atdabanian Stage IV excursion in Siberia (Brasier et al., 1994; Kouchinsky et al., 2007). Within the Arroyo Pedroche section, these positive $\delta^{13}C_{carb}$ values precede a plateau of -1.5‰, further consistent with values recorded from expanded sections of early Atdabanian age (Maloof et al., 2005; Kouchinsky et al., 2007). Thus, chemostratigraphy corroborates biostratigraphic assignment of the Pedroche Formation to the lower part of Cambrian Series 2, Stage 3. Moreover, correlation of the Pedroche $\delta^{13}C_{carb}$ values to a radiometrically calibrated Cambrian Terreneuvian–Series 2 $\delta^{13}C_{carb}$ curve suggests an absolute depositional age between 520.93 ± 0.14 Ma and 517.0 ± 1.5 Ma (Maloof et al., 2010b; Landing et al., 1998).

If interpreted as faithful recorders of the isotopic composition of contemporaneous seawater, the architecture and magnitude of $\delta^{13}C_{carb}$ variation within the three measured stratigraphic sections suggests they record overlapping but not entirely equivalent time intervals (Fig. 2). Specifically, isotopes imply that deposition of the Las Ermitas section correlates only with the upper half of the succession at Arroyo Pedroche. Detailed correlation with the Pilgrimage Road section is less clear. Many of the carbon isotopic values reported from Pilgrimage Road are more negative and display more point-to-point variability than those reported from either the Arroyo Pedroche or Las Ermitas sections. Carbonates at Pilgrimage Road are often nodular, massively recrystallized, and/or interbedded with siliciclastic strata; these textures and facies associations often result from, or are susceptible to, diagenetic recrystallization which, in the presence of organic remineralization, can impart more negative and scattered isotopic values. We note that $\delta^{18}O_{carb}$ isotopic values of the Pilgrimage Road section are not more negative than the other two sections (see Supplementary Data Table). Broadly, however, the stratigraphic trends measured at Pilgrimage Road resemble those at Arroyo Pedroche. In any event, the Pedroche Formation, as defined by lithostratigraphy, encompasses diachronous carbonate deposition.

The global boundary stratotype section and point (GSSP) for the Cambrian Terreneuvian–Series 2 boundary remains under consideration by the International Subcommission on Cambrian Stratigraphy (Peng and Babcock, 2011). Most workers propose to define this boundary at the first appearance datum of trilobites (Zhu et al., 2006; Babcock and Peng, 2007; Peng and Babcock, 2011) or various SSF taxa (Rozanov et al., 2011; Steiner et al., 2011). However, the concept of the first appearance datum has been criticized for potential

globally diachroneity (Landing et al., *in press*), due either to lithofacies-/sequence stratigraphic-bound fossil distribution (see, for instance, Holland, 1995) or provincialism and delayed ecological dispersion. For these reasons, Landing et al. (*in press*) propose to tie the Terreneuvian–Series 2 boundary to the positive $\delta^{13}C_{carb}$ excursion IV within the lower Atdabanian Stage of Siberia. The chemostratigraphic framework developed here for the trilobite, archaeocyath, and small shelly fossil bearing Pedroche Formation will assist in the correlation of the Ovetian Stage to other regions in which high-resolution biostratigraphy can be linked to chemostratigraphy. However, the difficulty in making detailed correlations between the Pilgrimage Road section to the Arroyo Pedroche type section—just kilometers away—provides a note of caution in applying chemostratigraphy to boundary definition. Without question, the strongest correlations—and, hence, boundary definition—will occur when bio- and chemostratigraphic data are considered together.

5. LITHOFACIES DESCRIPTIONS and PALEOENVIRONMENTAL INTERPRETATIONS

In the follow section, we describe the lithofacies comprising the Pedroche Formation, document the association of these lithofacies within each of the three measured stratigraphic sections, and interpret the environment of deposition. This sedimentological and stratigraphic framework will provide the context for quantifying the skeletal contribution to, and petrographic textures of, the carbonate lithofacies of the Pedroche Formation.

5.1 Lithofacies descriptions
5.1.1 Thrombolite facies and associated nodular limestone
　　　Calcimicrobial thrombolite (facies A; Fig. 3), herein referred to as thrombolite, occur with the characteristic mega- to meso-scale structures defined by Shapiro (2000). The simplest macrostructures appear as isolated, subspherical patches or 'head-like-shapes' (facies A-0; Fig. 4), 15-20 cm wide and up to 40 cm high, with densely packed, irregular-shaped mesoclots (1-2 cm wide; mesostructure 'a'; Fig. 4). These thrombolite heads occur interbedded with finely laminated siltstone, sandstone and thin interbedded ooid lenses (Fig. 4; see facies C1 below). Most commonly, thrombolite heads nucleated atop ooid lenses. These patches of thrombolite heads are smaller than those described as calyptra mounds by James and Debrenne (1980).
　　　Commonly, thrombolites aggraded to meter-scale megastructures within the Pedroche Formation, and these are characterized by both biohermal and biostromal geometries. Here, we subdivide Pedroche thrombolite bioherms according to their size, coeval facies-relationships and internal structure. The largest bioherms (facies A-I and A-II; Fig. 4), up to 2-3 m in diameter and 2.6 m high, resemble complexes elsewhere described as 'dilophoids' (see review in James and Debrenne, 1980). These geometries aggrade through the lateral and vertical stacking of smaller, subspherical head-like forms, generally 20-25 cm in diameter (facies A-I), but up to 50 cm in diameter toward the tops of bioherms (facies A-II). Small heads display dense, irregular-shaped mesoclots (1-2 cm wide; mesostructure 'a'; Fig. 4) whereas the largest heads include large, irregular mesoclots (10-15 cm wide; mesostructure 'd'; Fig. 4) that may contain archaeocyaths (mesostructure 'e'; Fig. 4). Within bioherms, individual thrombolites heads are surrounded by siltstone (Figs. 3 and 4). Moreover, larger bioherms occur as both isolated aggradations and as laterally and vertically stacked 'stratigraphic reefs' (*sensu* Dunham, 1970).
　　　Bioherms (facies A-I and A-II) grade laterally into nodular limestone and fine siltstone interbeds. The nodular limestones (facies B; Fig. 4) have a mottled texture imparted by the high

density of small, rounded thrombolite mesoclots (<5 mm, commonly ~ 2 mm; mesostructure 'b'; Fig. 4). Toward the top of some bioherms, the mesostructure of nodular limestone displays develops columnar/digitate mesoclots, some of which branch (mesostructure 'c'; Fig. 4). These columnar and digitate mesoclots may be scoured by oolitic grainstone. The largest bioherm complexes are usually onlapped by parallel laminated siltstone and sandstone and ripple cross-bedding sandstone, revealing cm- to decimeter-scale synoptic relief during bioherm accretion.

Small bioherms (facies A-III; Fig. 4), usually 1 m in diameter and up to 1 m in height (Fig. 3a), have an internal structure equivalent to A-I bioherms composed of small, irregular mesoclots (mesostructure 'a'; Fig. 4). Like their larger counterparts, these bioherms commonly nucleated above channelized lithosomes of ooid and oncoid grainstone (facies C2 below). Ooid channel deposits (up to 70 cm thick), wavy-to-hummocky laminated siltstone, and ripple cross-bedded sandstone drape and flank the margins of small bioherms, and interbed laterally with small bioherms.

Biostromal geometries occur as plano-convex, lenticular beds up to 2 m-wide and 60 cm-thick (facies A-IV; Fig. 4) and as thick, vertically stacked, tabular beds (facies A-V; Fig. 4). Lenticular biostromes display an internal structure composed of small, sub-spherical heads of densely packed, irregular mesoclots (mesostructure 'a') and, occasionally, larger heads with large, irregular mesoclots with rare archaeocyaths (mesostructure 'e'). These lenticular biostromes commonly appear above the top of coarsening- and thickening-upward sequences from finely laminated siltstone to interbedded siltstone and sandstone to hummocky cross-bedded sandstone. They also occur above thin, massive lenses (facies C1), small, channelized lithosomes (facies C2), and planar cross-bedded tabular beds (facies C3) of ooid and oncoid grainstone (see facies description below).

Tabular biostromes do not display the characteristic internal structure of amalgamated subspherical heads. Rather, these beds display a massive internal texture with diffuse, wavy silt intercalations, fenestral cavities, a variable density of mesoclots, and irregular red sedimentary infillings (mesostructures 'h', 'i' and 'j'; Fig. 4). Outcrop observations indicate that fenestral cavities, up to 2 cm wide, account for ~5% to 20% of tabular biostrome beds whereas the red irregular infillings may comprise up to ~30-40% of these beds. Some thick, biostromal beds display an increase in the density of mesoclots, silt content, and the density of fenestral and irregular cavities from the base to the top of each bed (gradational transition from 'h' to 'j'). Accompanying the increase in red, sedimentary infillings, tabular biostrome beds show a characteristic vertical change from grayish to reddish colors. Large, irregular mesoclots with archaeocyaths (mesostructure 'e') may also occur. Thrombolite biostrome tops occasionally develop columnar stromatolites that interfinger laterally with ooid grainstone.

In thin-sections with exceptional fabric retention, petrography reveals that thrombolite mesoclots are composed of the calcimicrobes *Epiphyton*, *Renalcis*, and, rarely, *Girvanella* that appear as both intergradations and intergrowths from one morphotype to another at a sub-mm scale (Fig. 5a,b; Pratt, 1984). Aggrading neomorphism and/or secondary dolomitization obscures the primary texture of the matrix between micritic mesoclots. Crenulated-to-wispy dissolution seams with siliciclastic and iron oxide stylocumulate are common to this lithofacies. Millimeter-scale veins of coarse calcite spar often dissect the thrombolite lithofacies.

Within the thrombolite facies, archaeocyath fossils occur both surrounded by the grey, fine-grained matrix between mesoclots (mesostructure 'd'; Fig. 3d) and within large mesoclots (mesostructure 'e'). The maximum density of archaeocyaths in thrombolite facies was observed in *ex situ* blocks at the Arroyo Pedroche section (Fig. 2, covered interval between 68 m and 81 m) that were displaced during construction of a local road. These *ex situ* blocks display two

mesostructures ('f' and 'g'; Fig. 4), where large irregular mesoclots are surrounded by mm- to cm-scale lenses of oolite and siltstone. Within these blocks archaeocyaths developed a secondary branching modular framework (described by Moreno-Eiris, 1987a, b, c, d) and we estimate, based on outcrop appearance, that archaeocyaths account for up to 20-30% of rock volume,. In general, however, and throughout *in situ* strata of our measured sections, archaeocyaths represent a more minor component of this lithofacies.

5.1.2 Ooid, oncoid and peloid grainstone

Lithofacies C consists of light grey to mauve weathering, medium-to-thick beds of well-sorted ooid, oncoid, and/or peloid grainstone (Fig. 6). These grainstone beds occur with massive, lenticular geometries (facies C1; Fig. 4); as channelized lithosomes (facies C2; Fig. 4); and as tabular beds with planar cross-bed sets (facies C3; Fig. 4). Individual ooids range from 0.5–1.0 mm in diameter (Fig. 6a). Petrographic examination reveals three distinct cortical fabrics. Most commonly, ooids display a fabric-destructive dolomitization by euhedral crystals (Fig. 7a-c). This texture indicates dissolution of the primary cortical mineralogy, leaving casts of nearly circular morphology later filled with cement (oomolds). More rarely, ooids have a micritized cortex (Fig. 7d). In some instances, these reveal faint concentric laminations and/or the ghosts of radially oriented crystals (Fig. 7e), suggesting that micritization occurred at the expense of the primary cortical fabric. Under cross-nichols, micritic ooids display a pseudo-uniaxial extinction cross. Regardless of preservation texture, few ooids retain discernable nuclei (Fig. 7). Such an absence suggests a nucleus of carbonate that dissolved along with the primary cortices. Rarely, the interiors of dolomitized ooids include a cluster of equant, anhedral microspar crystals, suggesting, perhaps, that ooids nucleated from peloids (Fig. 7b).

We observed a second set of structureless, micritized grains, 0.1–1.0 mm in diameter, with morphologies that deviate from spherical. We classified these as peloids. Peloids are generally ovoid, whereas coarse-grained peloids appear nephroid and, rarely, irregular in outline (Fig. 7f). A fibrous, isopachous cement often envelopes individual grains, displacing an inferred primary grain-to-grain contact (Fig. 7). Given the history of fabric-destructive recrystallization apparent from ooid textures, it is possible that grains classified as peloids based on their preserved texture originated as oncoids. Unambiguous oncoids are present as mm–cm, oblate-to-irregular shaped, sub-rounded micritized grains (Fig. 6b). Alternatively, some of these peloids may be superficial ooids that nucleated around irregularly shaped skeletal grains.

Skeletal clasts are rare within the ooid/oncoid/peloid grainstone facies (Fig. 5). Within all samples thin-sectioned from sections AP and PR, only trilobites (Fig. 5c), calcitic brachiopods (Fig. 5d), and SSFs (Fig. 5e) were identified within the grainstone lithofacies; archaeocyaths were absent from bioclastic debris. When present, skeletons and bioclasts are molded by an equant, microspar, and are commonly enveloped by isopachous cements (Fig. 5). Trilobite carapaces and cortoids of trilobite incurved margins are replaced by rectangular-to-blocky dolomite (Fig. 5c).

5.1.3 Interbedded carbonate mudstone; bioclastic wackestone; archaeocyathan floatstone, packstone, and *rudstone; and siliciclastic siltstone*

Facies assemblage D consists of massive, neomorphosed carbonate mudstone; bioclastic wackestone; and intergrading archaeocyathan floatstone, packstone and rudstone interbedded with abundant crenulated-to-stylolitic, parallel, sub-parallel, and anastomosing laminae and beds of red siliciclastic siltstone imparting an amalgamated stylonodular to stylobedded fabric (Figs. 4 and 8a-c). Individual facies occur either with gradational-to-sharp contacts over a cm-to-mm

scale, or as micronodules delineated by dissolution seams enriched in siliciclastic stylocumulate. Field observations indicate that carbonate comprises ~50–80% of this lithofacies, averaging 60–70%; however, for short stratigraphic intervals, siltstone laminae and beds may comprise up to ~80% of rock volume. Rarely, these lithologies compose the clasts of intraclastic breccias. Archaeocyathan clasts, which range from 0.5–3 cm in diameter, are oriented randomly and aligned along their elongate axis (Fig. 8b,c).

Petrography reveals three distinct neomorphic carbonate spar fabrics. The first is an inequigranular, xenotopic, reddish-pink microspar hosting 5–10% brown-to-opaque, rectangular, silt-sized clay mineral grains and sub-rounded Fe-oxide crystals, perhaps after pyrite (mcr1; Fig. 8d). This fabric is interpreted as a neomorphosed silt-bearing micrite. A second common fabric comprises a drusy-to-equant mosaic of xenotopic microspar lacking siliciclastic grains but, at times, hosting < 5% light-green, rectangular lathes of glauconite (mcr2; Fig. 8e). This fabric represents a variably fabric destructive to fabric retentive early burial cement. Less commonly, a third fabric of equigranular, hypidiotopic-to-idiotopic coarse spar with twinned-lamellae occurs as pockets within fabric mcr2, forms recrystallization halos around archaeocyath skeletal clasts, or veins that cross-cut other matrix fabrics (sp; Fig. 8f). We interpret this fabric to have formed during later stage fluid flow that neomorphosed the drusy cement, with flow preferentially running through high porosity conduits provided by archaeocyath skeletons.

Archaeocyath skeletal preservation occurs through multiple pathways (Fig. 9). Drusy microspar (mcr2, but lacking glauconite) typically molds the outer wall, inner wall and septa of individual archaeocyaths (Fig. 9b-d). Rarely, microcrystalline hematitic overgrowths, known as frutexites, rim the exterior of the outer wall (Fig. 9a). (Frutexites has been described from Proterozoic to Recent marine, continental, and subterranean depositional environments within stromatolites, hardgrounds, microbial limestones, cavities, caves, and Neptunian dikes; most authors consider Frutexites to be a bacterial-induced texture (see review in Rodríguez-Martínez, 2011)). Commonly, a slightly coarser drusy microspar (mcr2) or an optically twinned, coarse spar (sp) molds the intervallum (Fig. 9c,d); more rarely, the intervallum may be filled with reddish-pink microspar (mcr1; Fig. 9b) or include both mcr1 and mcr2 within the same specimen (Fig. 9c). Likewise, the central cavity may be infilled by mcr1 (Fig. 9b,c); however, more commonly among smaller specimens, the central cavity is molded by drusy microspar (mcr2) or a coarse spar (sp; Fig. 9d). The petrogenesis of archaeocyath preservation is apparent from Figure 9b-c. Post-mortem, the intervallum and central cavity of archaeocyathan clasts are filled, to varying degrees, by siliciclastic-bearing carbonate silt (mcr1). Subsequently, primary skeletal porosity is occluded by a drusy microspar cement (mcr2) or coarse spar (sp).

Small shelly fossils are always molded by a drusy microspar (mcr2; Fig. 10). Within this lithofacies, microbial fabrics are rare but, when present, include mm-scale hematitic stromatolites (Fig. 9a) and filamentous, oncolitic halos around archaeocyathan bioclasts (Fig. 9b). No echinoderm ossicles, and few trilobite carapaces, were observed within representative thin-sections of this lithofacies.

5.1.4 Massive grainstone and recrystallized carbonate

This facies consists of thin to thick tabular or irregular-to-wavy beds of very fine- to medium-grained grainstone, nodular carbonate and thick to very-thick beds of massive, and finely-to-coarsely recrystallized and/or vuggy dolomitized carbonate.

5.1.5 Fine-grained siliciclastic rocks

This facies consists of very thin to thin beds of shale and planar laminated and ripple cross-laminated siltstone as well as thin to medium, planar-to-undulose beds of very fine to medium-grained, micaceous quartz sandstone which may be massive, planar laminated, ripple cross-laminated, or swaley-to-hummocky cross-laminated and cross-stratified.

5.2 Lithofacies associations

5.2.1 Cerro de Las Ermitas section

At the Cerro de Las Ermitas study area, carbonates of the Pedroche Formation transgressed over and infilled meter-scale paleotopographic relief incised into andesite of the underlying San Jerónimo volcano-sedimentary complex (Fig. 2). A complex cavity-dwelling calcimicrobial and skeletal community found on this paleosurface is described thoroughly by Vennin et al. (2003) and Perejón and Moreno-Eiris (2007).

Within the same study area, a decameter-scale bioherm directly, but unconformably, overlies these andesites (Zamarreño and Debrenne, 1977; Moreno-Eiris, 1987). Moreno-Eiris (1987) differentiated seven lithofacies along three stratigraphic transects: i) polymictic conglomerates (with rounded, pebble- to boulder-size clasts of andesite, metaquartzite, and shale) and violet siltstone; ii) micaceous, quartz-rich, laminated siltstone; iii) siltstone with calcareous nodules; iv) micritic limestone; v) reefal limestone (up to 12 m thick) and small calcimicrobial mounds; vi) nodular peri-reefal limestone; and vii) carbonate sedimentary breccia. The Cerro de Las Ermitas stratigraphic section of this study (LE; Figure 2) partially overlaps the section described by Moreno-Eiris (1987; section VII', up to their 40 m). The 'interbedded carbonate mudstone, bioclastic wackestone and archaeocyathan floatstone, packstone and rudstone and siliciclastic siltsone' lithofacies assemblage (facies D) of this study corresponds to the nodular peri-reefal limestone and siltstone with calcareous nodules facies described by Moreno-Eiris (1987). We note that while our Cerro de Las Ermitas section did not directly transect an archaeocyath framework reef, bioherms were observed directly above the section. We do not include these bioherms in our measured section because dense vegetation precluded confident stratigraphic placement.

5.2.2 Cerro de Las Ermitas environmental interpretation

The interlaminated fine-grained carbonate (mudstone and wackestone) and siliciclastic siltstone lithologies accumulated predominately through the settling of suspended fine grains during very low energy conditions. The changing abundance of carbonate versus siliciclastic silt reflects the temporally-variable influx of terrigenous material diluting and/or suppressing background carbonate production. In contrast, coarse-grained carbonate lithologies reflect higher-energy depositional episodes that entrained reef organisms, re-worked, and winnowed them, as evidenced by deposits of parallel-oriented whole and partial archaeocyath clasts (Fig. 8b). Localized brecciation within this lithofacies likely resulted from the collapse of the flanks of over-steepened calcimicrobial reefs. We interpret this lithofacies assemblage as an inter-reef and reef-flank (talus) deposit.

5.2.3 Pilgrimage Road section

The Pedroche Formation is ~133 m thick at this stratigraphic section; however, there are no biostratigraphic zonations determined for this section to correlate to the Arroyo Pedroche or Cerro de Las Ermitas sections. Within this section, the lowermost strata of the Pedroche Formation (0 – 45 m) are dominated by siliciclastic facies with minor interbeds of carbonate.

These siliciclastic lithologies are stacked in meter-scale parasequences of planar and ripple cross-laminated siltstone and very fine- to fine-grained micaceous quartz sandstone with and without lime mudstone nodules. Flaser bedding occurs rarely within the basal 25 m of the section. Beds of massive and ripple cross-bedded fine- to medium-grained quartz sandstone, beds and lenses of massive (facies C2) and ripple cross-bedded (facies C3) ooid/oncoid/peloid grainstone, and thrombolites (facies A-0 and A-IV) intercalate with these fine-grained siliciclastic lithologies.

At ~45 m, the carbonate mudstone nodules within a 2.5 meter-thick siltstone/sandstone bed increase in abundance, grading into a carbonate interval from 47.5 – ~71 m. Carbonate textures within this interval include: interbedded massive recrystallized limestone; vuggy, coarse-crystalline dolomite; and one ~3 meter-thick massive, recrystallized thrombolite (facies A-II).

Cyclic interbedding of lithofacies occurs from ~71 m to the top of the measured section. (Here, we use the term cycle to describe repetition of lithologies, not to invoke a particular time-scale or depositional mechanism (*sensu* Myrow et al., 2012).) At Pilgrimage Road, cycles include: (1) micaceous siltstone and very fine-grained quartz sandstone, (2) massive to cross-bedded ooid/oncoid/peloid grainstone (facies C2 and C3) followed by (3) very thick, massive thrombolite biostrome (facies A-V) interbedded and draped with siltstone. Variations on this generalized lithologic cycle include the absence of either the fine-grained siliciclastics or the ooid/oncoid/peloid grainstone lithofacies. The thrombolite facies contains rare archaeocyaths. Zamarreño (1977) described the cyclic interbedding of these lithofacies, as well as the geometry of thrombolite mounds, in further detail.

5.2.4 Arroyo Pedroche section

Previously, the Arroyo Pedroche section was divided into two members (Perejón et al. 1996), and here we focus our work on Member 1. The Arroyo Pedroche section comprises mixed siliciclastic and carbonate lithologies, both non-cyclically and meter- to decameter-scale cyclically (serially repeated) bedded (Fig. 2). At Arroyo Pedroche, the lowermost ~19 m of the Pedroche Formation consist of shale and siltstone with minor intercalations of bedded thrombolite (facies A-0 and A-IV), nodular limestone (facies B), and ooid/oncoid/peloid grainstone (facies C1). Towards the top of this interval, ripple and hummocky cross-stratified siltstone and fine- to medium-grained sandstone beds occur along with rare beds of massive ooid grainstone (facies C3). Massive, recrystallized carbonate crops out between 19 and 31 m, yet relict textures within this interval indicate a primary thrombolite texture (facies A-1).

From 31 – 39 m, the Pedroche Formation records the vertical accretion of six thrombolite bioherm complexes (facies A-I and A-II) that grade laterally into, and intercalate with, coeval nodular limestone (facies B) and parallel laminated shale and siltstone. Thrombolite bioherms nucleated atop both siliciclastic beds and ooid/oncoid/peloid grainstone channel deposits (facies C2). Generally, parallel and ripple cross-laminated, very fine-grained sandstone caps these bioherm complexes, but occasionally channelized ooid/oncoid/peloid grainstone erode into the top and margin of bioherms.

From ~40 – 50 m, the section comprises non-cyclic intercalations of: (1) planar laminated shale and siltstone, and planar laminated to ripple cross-laminated very fine-grained sandstone; (2) beds, channels (facies C2), and lenticular bars (facies C3) of ooid/oncoid/peloid grainstone; and (3) small, isolated and amalgamated thrombolite bioherms (facies A-III) typically surrounded by bedded, fine-grained siliciclastic lithologies.

The stratigraphic interval from 50 – 60 m corresponds to a coarsening- and thickening-upward succession of finely laminated siltstone, parallel and ripple cross-laminated sandstone

and hummocky cross-stratified sandstone. Lenticular thrombolites (facies A-IV) nucleated above these sandstone beds and were capped by finely-laminated siltstone. The final development of thrombolite bioherms (facies A-III and A-II) at the Arroyo Pedroche section, from ~60 – 65 m and in *ex situ* blocks within a covered interval up to 81 m, aggraded in association with ooid/oncoid grainstone (facies C3) and were subsequently draped by siltstone laminae that grade upwards into trough cross-stratified sandstone.

Cyclic interbedding of facies is more strongly developed from 81 – 92 m. These cycles consist of a basal, siliciclastic-dominated interval and an upper, carbonate-dominated interval. The generalized succession of siliciclastic lithologies within cycles includes: (1) interbeds of laminated shale and siltstone and/or (2) interbeds of laminated-to-swaley siltstone and very fine-grained sandstone grading into (3) swaley, hummocky, or ripple cross-laminated, very fine- to medium-grained, amalgamated sandstone. In turn, the coarser, cross-stratified siliciclastic lithologies are commonly interbedded with, or overlain by, carbonate facies that may include: (4) cross-bedded or massive ooid/peloid/oncoid grainstone and (5) lenticular thrombolites (facies A-IV). Broadly these mixed siliciclastic-carbonate cycles represent upward-coarsening cycles. We note, however, that interbedding of siliciclastic lithologies may occur without a discernable coarsening-upward succession, or instead, display a distinct shaling-upward succession. In this upper cyclic section, wispy-to-crenulated physical dissolution seams with siliciclastic stylocumulate are common within carbonates, and increase in density near cycle tops.

Throughout the remaining strata of the Arroyo Pedroche section (92 – 138 m), thrombolite biostromes (facies A-V) are common and nucleate from massive to planar cross-bedded ooid/oncoid/peloid grainstone (facies C3) and, more rarely, sandstone. Within this interval, the transition from thrombolitic to columnar stromatolitc texture near the top of bioherms is common. Generally, however, thrombolites display typical mesostructure fabrics with fenestral cavities.

5.2.5 Arroyo Pedroche and Pilgrimage Road environmental interpretations

Facies associations of the Pedroche Formation at the Pilgrimage Road and Arroyo Pedroche sections record broadly similar depositional environments. The base of both stratigraphic sections record predominantly siliciclastic sedimentation with only minor carbonate interbeds. Within the Arroyo Pedroche section from 0 – 14 m, the interlaminated and interbedded shale, siltstone, and fine sandstone without macroscopic sedimentary structures indicate suspension deposition of fine-grained siliciclastic particles entrained in dilute turbidity currents. We interpret these lithologies to record sediment accumulation in an offshore shelf or distal ramp setting. In contrast, the introduction of macroscopic sedimentary structures within siltstone and sandstone above 14 m—including hummocky, swaley, and ripple cross-lamination—record traction deposition from gravity waves. Such sedimentary structures within well-sorted, amalgamated beds are common in shoreface depositional environments. Thus, the base of the Arroyo Pedroche section records an upward-shoaling succession from a calm, deep-water setting to one influenced by tide, wave, and storm activity.

The basal meter-scale siliciclastic-parasequences of the Pilgrimage Road section (0 – 45 m) include parallel and ripple cross-laminated siltstone and sandstone, and wavy and flaser bedding structures. Like the Arroyo Pedroche section, the minor interbeds of massive lenses of ooid grainstone (facies C3), here interpreted as storm-induced gravity flow deposits, and the aggradation of isolated thrombolites (facies A-0 and A-IV) represent the maximum advance of the carbonate system onto the middle/upper shoreface. We interpret the lower ~25 meters of the Pilgirmage Road section, below the common occurrence of thrombolites, to record a shallowing

upward succession displaying an increase in higher-energy facies (e.g., wave-rippled siltstone, sandstone, and ooid/oncoid grainstone) and a reduction of fine-grained, suspension settled siliciclastic input. However, this shallowing resulted in deposition transitioning from lower/middle to upper shoreface conditions rather than from offshore to shoreface deposition as recorded within strata at the Arroyo Pedroche section.

Within both the Arroyo Pedroche and Pilgrimage Road sections, the reduction in siliciclastic influx likely facilitated the colonization of the seafloor by calcimicrobial communities and the aggradation of thrombolites (facies A-0 and A-IV thrombolites found within the basal meters of both sections). At Arroyo Pedroche, this shallowing preceded the maximum development of laterally and vertically stacked thrombolite bioherms with centimeter- to decimeter-scale synoptic relief (31 – 39 m). At Pilgrimage Road, this shallowing preceded the deposition of carbonates for which recrystallization has since destroyed primary textures. Hence, we do not offer an interpretation of depositional environment for these strata.

We interpret the depositional environment of Arroyo Pedroche strata from 31 – 49.5 m as a thrombolite mound-and-channel facies. Here, fine-grained siliciclastic lithologies onlapped onto, and scoured the margins of, thrombolites bioherms. The continuous disaggregation and erosion of thrombolite into small, rounded micritc grains (peloids) contributed to accumulation of nodular limestone (facies B) surrounding the bioherms. In turn, both the thrombolite bioherms and the surrounding peloidal, nodular limestones were sporadically scoured by channelized ooid and oncoid deposits.

Massive, planar-laminated and ripple cross-laminated, undulatory-bedded carbonate grainstone, and massive carbonate without discernible texture, record a combination of traction transport and suspension deposition. These lithologies are common in shallow, subtidal depositional environments. Well-sorted, cross-bedded ooid/oncoid/peloid grainstone beds reflect traction deposition from high-energy flow capable of winnowing carbonate and siliciclastic mud, silt and fine sand grains. We interpret these lithologies as migrating shoals and/or sheets that prograded onto deeper subtidal lithologies (i.e., siliciclastic sands and thrombolite bioherms).

In turn, the migration of siliciclastic sand shoals and ooid channels and shoals influenced the geometry of thrombolite growth. Large thrombolite bioherms (facies A-I and A-II) accreted during coeval suspension deposition of silts. In contrast, the lateral and vertical accretion of small bioherms (facies A-III) was stymied by the physical erosion and cessation of carbonate production by migrating siliciclastic sand shoals and subtidal oolitic channels. The presence of swaley and hummocky cross-laminae within siliciclastic sandstone reflects wave-generated bedforms developed during storms. In the intervening calm periods, the sandy seafloor was continually and densely recolonized by calcimicrobes, allowing lenticular thrombolites to develop, before subsequent influxes of suspended siliciclastic sediment smothered them during storms.

We interpret the uppermost meter-scale thrombolite bioherms (facies A-II and A-III) at the Arroyo Pedroche section to have grown in shallow, protected back-shoal environments behind and between ooid/oncoid/peloid bar deposits (facies C3). The widespread development of fenestral cavities within these bioherms, the increase in silt intercalations within thrombolitic textures, and the transition from thrombolite to columnar stromatolite at the top of these bioherms all support the interpretation of a shallow, back-shoal environment.

The interfingering and interbedding of siliciclastic sands, oolitic carbonates, and thrombolite bioherms within the mound-and-channel environment speaks to a contiguous spatial distribution of these lithofacies along an ancient mixed siliciclastic–carbonate shoreface. Evidence for subaerial exposure is absent in both sections. From this we interpret that sediment

influx did not consistently outpace the creation of accommodation space. Likewise, the common occurrence of macroscopic sedimentary structures formed from traction deposition indicates that the creation of accommodation space did not significantly outpace sediment accumulation, which would result in shoreface retrogradation and transition into an offshore depositional environment. Thus, we interpret the alternation between siliciclastic-dominated and carbonate-dominated sedimentation within the mound-and-channel facies to reflect the lateral migration of lithofacies rather than major changes in accommodation space and facies belts.

In contrast, when mixed siliciclastic–carbonate lithologies occur together in continuous, upward-coarsening cycles (as above 81 m at Arroyo Pedroche, and above 71 m at Pilgrimage Road), we interpret these as upward-shoaling successions. Above the major covered interval at Arroyo Pedroche, the basal medium-grained sandstone (81 m) of the cyclic-interbedded section includes hummocky cross-stratification. The re-introduction of this sedimentary structure indicates a deepening to a storm-dominated shoreface. Above this cycle, both the transgressive siliciclastics that define the base of each cycle and overlying ooid grainstone beds include ripple cross-stratification indicative of deposition above fair-weather wave base. We note, however, that the deviations from simple upward-coarsening siliciclastic successions, such as fining-upward patterns or frequent alternations between suspension and traction deposited sediments, reflect a more complex sediment accumulation pattern than simple shoreface progradation.

The architecture of thrombolite facies changes significantly between the lower and upper portions of both the Arroyo Pedroche and Pilgrimage Road sections. Within the basal ~71 m at AP, and the basal ~45 m at PR, both intervals of siliciclastic-dominated offshore to lower shoreface deposition, thrombolites aggraded as bioherms with significant synoptic relief. In contrast, in the upper, cyclically bedded stratigraphy, thrombolite facies developed with biostromal geometries, often interbedded with siltstone. Biohermal thrombolites can aggrade when water depth exceeds synoptic relief. As a corollary, the development of biostromal morphologies could reflect limited accommodation space, characteristic of very shallow to nearly emergent depositional environments. However, the presence of siliciclastic silt interlaminae and drapes disrupting the aggradation of thrombolite bioherms and biostromes suggests that the morphology of thrombolite accretion was also controlled by the relative rates of carbonate precipitation versus siliciclastic influx (Cowan and James, 1993; see analogous discussion of stromatolite aggradation in Grotzinger and Knoll, 1999). Thus, rather than strictly associate thrombolite facies architecture with a flow-regime or water depth, we assume that siliciclastic influx also influenced the morphology of thrombolite accretion. The common occurrence of ooid/oncoid/peloid grainstone and sandstone beds underlying thrombolites suggests that a rough substrate and a slightly elevated stable surface, were favorable conditions for colonization of the seafloor by calcimicrobes and subsequent thrombolite growth.

6. THE CHARACTER OF PEDROCHE FORMATION CARBONATES

6.1 Carbonate versus siliciclastic lithofacies of the Pedroche Formation

The percent contributions of carbonate lithofacies to the three stratigraphic sections of the Pedroche Formation are reported in Table 1. Thrombolite facies comprise 27% and 26% of the Arroyo Pedroche and Pilgrimage Road sections, respectively. Ooid/oncoid/peloid grainstone comprise 3% and 6% of the AP and PR sections, respectively. Other carbonates (i.e., massively recrystallized strata) account for 14% and 15% of the AP and PR sections, respectively. Siliciclastic lithologies make up the remaining 56% and 53% of the AP and PR sections,

respectively. When calculated on a carbonate-normalized basis, thrombolites, ooid/oncoid/peloid grainstone, and other carbonate lithofacies make up 60%, 8%, and 32%, respectively, of the AP section and 55%, 13%, and 31%, respectively, of the PR section.

Given the mm- to cm-scale transition between lithologies in the interbedded carbonate mudstone, bioclastic wackestone, archaeocyathan floatstone–packstone–rudstone and siliciclastic siltstone lithofacies (facies assemblage D) of the Cerro de Las Ermitas section, we do not attempt to quantify the percent siliciclastics versus carbonates, or the percent of individual carbonate lithologies beyond the field observation estimates reported with the lithofacies descriptions.

6.2 Quantifying skeletal contributions to, and fabric components of, carbonate facies of the Pedroche Formation

Our raw point-count data are summarized in Table 2. In the following discussion, we report the calculated average percentage of a constituent skeletal or fabric component within a lithofacies unless otherwise noted (summarized in Table 3).

The percentage of skeletal material contributing to carbonate lithofacies of the Pedroche Formation, as determined from the point count data in Table 2, is shown in Fig. 11. Total skeletal contribution peaks at 21.5% (average 18±3%; Fig. 11a) in thin-sections identified as archaeocyathan floatstone, packstone, or rudstone lithologies within facies assemblage D. In contrast, total skeletal contributions to thin-sections classified as bioclastic wackestone or carbonate mudstone in facies assemblage D range from 3–9% and 0–2%, respectively (Fig. 11a). Within the archaeocyathan floatstone–packstone–rudstone lithofacies, archaeocyaths are more abundant than SSFs (Fig. 11b), with archaeocyaths averaging 11±4% and SSFs averaging 4±2%. In contrast, within bioclastic wackestone and carbonate mudstone lithofacies, archaeocyaths are, on average, less abundant than SSFs (Fig. 11c). No thin sections of the thrombolite facies included a quantifiable skeletal contribution (Fig. 11a). Likewise, of the ooid/oncoid/peloid grainstone samples analyzed, only one revealed a discernable skeletal contribution (2%; Fig. 11a).

The percent composition of all quantitatively important (i.e., > ~1%) constituents of each of the carbonate lithofacies assemblages of the Pedroche Formation is depicted in Fig. 12. In addition to the variable skeletal contribution discussed above, micrite (82±11%) and siliciclastic clay and/or silt (8±8%) dominate the composition of facies assemblage D (Fig. 12a); in contrast, microbial textures (e.g., hematitic stromatolitic laminae and frutexites) contribute a maximum of 9%, but typically much less (0.6±2%; Fig. 12a; see photomicrograph in Fig. 8). The thrombolite lithofacies is composed entirely of clotted micrite (36±6%) set within a microspar matrix (herein interpreted as neomorphosed micrite; 50±5%; Fig. 12b). Similarly, the ooid/oncoid/peloid grainstone lithofacies is composed almost entirely of either ooids (39±18%), oncoids/peloids (5±9%, respectively) and sparry cement (47±9%; Fig. 12c).

6.3 Comparing the nature of carbonate production within the Pedroche Formation to other Lower Cambrian, archaeocyathan-bearing carbonate platforms

The assignment of the Pedroche Formation to Cambrian Series 2, Stage 3 provides context for comparing Pedroche carbonate production in general, and skeletal contribution in particular, to contemporaneous carbonate platforms and archaeocyathan bioherms. First, however, we must address how well our point-count data estimate skeletal contributions to these lithofacies. All Pedroche Formation samples reveal some evidence of fabric destructive

diagenesis. The subset of thin-sections analyzed in detail display the least pervasive fabric-destructive diagenesis such that point counts of textural fabrics and fossil occurrences should best approximate the primary depositional texture. Nevertheless, the results presented here are necessarily minimum estimates of the primary carbonate constituents (e.g., skeletons and coated grains) or maximum estimates of secondary textures (e.g., cements). Even when primary matrix microfabrics are difficult to discern, however, original skeletal elements often retain their diagnostic features (e.g., Fig. 9a). Finally, we note that the most fossiliferous strata (archaeocyath rudstone and floatstone) observed in our field area were *ex situ* blocks within the Arroyo Pedroche section in an interval without clear biostratigraphic or chemostratigraphic relationship to the Las Ermitas section. While the most fossiliferous samples point counted within this study approach the percent archaeocyath skeletal volumes of these *ex situ* lithologies that we estimated by eye, our point-count samples may ultimately underestimate the total skeletal abundance by several percent.

The most pervasive fabric-destructive fabrics appear in the thrombolite facies, hence our limited point-count observations (n=5). Despite field observation of archaeocyaths (and other skeletons) associated with the thrombolite lithofacies (Fig. 3d), none of the thin-sections analyzed included a quantifiable skeletal contribution (Fig. 11a, 12b). Likewise, only one thin-section from the grainstone lithofacies included a quantifiable skeletal contribution (Fig. 11a, 11c). It is possible that fabric-destructive recrystallization caused point count data to underrepresent skeletal contribution to these lithofacies. We prefer, however, the interpretation that while archaeocyath and other skeletal elements are present within this lithofacies, their absence (or low abundance) from point-count data correctly implies limited abundance or, at the most, spatially-discrete enrichment in skeletal clasts that reflects a low total skeletal volume in these lithofacies.

Total skeletal contribution within the archaeocyath-bearing inter-reef and reef-flank facies (assemblage D) at Las Ermitas is similar to that determined by Hicks and Rowland (2009) for microbial bioherms of the Cambrian Series 2, Stage 3–4 Xiannudong Formation, Yangtze Platform, southern China as well as by Pruss et al. (2012) for archaeocyathan patch-reefs of the Cambrian Series 2, Stage 4 Forteau Formation, southern Labrador, Canada (Fig. 13a). Likewise, the percentage of total skeletal material representing archaeocyaths (Fig. 13b) versus all other fossils (Fig. 13c) is similar between these localities, with the notable exception of higher (up to 38%) archaeocyath abundance reported by Rowland and Gangloff (1988) within microbial-boundstone of the Cambrian Series 2, Stage 3 lower Poleta Formation, western Nevada, USA. We note, however, that the percent archaeocyath abundance determined by Rowland and Gangloff (1988) derives from volumetric determinations via tracing methods. Results from tracing methods overestimate skeletal contribution in comparison to the grain-solid point count method employed in both this study and by Pruss et al. (2012) and, therefore, cannot be directly compared to these studies. More generally, Debrenne (2007) has estimated that while the percent contribution of archaeocyaths to lower Cambrian bioherms can be as high as the 38% reported by Rowland and Gangloff (1988) in high energy reef crests, it is more commonly 13% or less in lower energy settings similar to those interpreted for the Pedroche Formation.

Taken together, thin-section point-counts of fossil abundance and identity within Cambrian archaeocyathan–bearing inter-reef and reef-flank facies (facies assemblage D) provide consistent views on reef ecology. Most lower Cambrian bioherms are calcimicrobe-bearing microbialites that contain archaeocyaths. Maximum skeletal abundance is similar at the three localities for which quantitative data are available (Fig. 13a), confirming previous interpretations that archaeocyath-bearing microbial reefs represent important but spatially limited loci of

carbonate production (Rowland and Gangloff, 1988; Hicks and Rowland, 2009; Pruss et al., 2012). Moreover, skeletal carbonate production is partitioned amongst archaeocyath and other skeletal taxa in a consistent ratio for all three localities (Fig. 13d). Thus, if archaeocyaths were not actively displacing other taxa from ecological niches, the evolution and expansion of the Archaeocyatha during Cambrian Series 2 likely buoyed skeletal carbonate production beyond the low diversity, low abundance observed in other places and at other times in the early Cambrian (Pruss et al., 2010). Yet, even in lower Cambrian lithologies bearing archaeocyaths, skeletons do not play the depositional role that they do later in the Paleozoic Era (Rowland and Gangloff, 1988; Hicks and Rowland, 2009; Pruss et al., 2012).

One significant difference between the Pedroche Formation and the Forteau Formation (Pruss et al., 2012) and, to a lesser extent, the Xiannudong Formation (Hicks and Rowland, 2009), is the minimal occurrence of skeletal material in Pedroche grainstone lithologies. Pruss et al. (2012) found up to 20.5% (average 12.4%) skeletal material in grainstone flanking archaeocyathan reefs, whereas we found skeletons in only one thin-section (of nine analyzed) with a total skeletal contribution of 2% (Fig. 11a). Grainstone shoals and sheets represent dynamic, high-energy depositional environments where rapidly changing wave-energies often winnow skeletal fragments into coarse lag deposits. Thus, for sedimentological reasons, we might expect high variance in the skeletal contribution to grainstone facies. Pruss et al. (2012) identified echinoderms as the major constituent of grainstone skeletal debris, whereas no echinoderm fossils were observed in Pedroche Formation thin-sections. Both fossils and molecular clocks indicate an initial diversification of echinoderms during Cambrian Series 2 (Peterson et al., 2004; Bottjer et al., 2006), but early taxa appear to have been facies bound, including, in the case of helicoplacoids, to siliciclastic facies (Smith, 1985; Dornbos and Bottjer, 2000). Thus, differences from one platform to another may well reflect environmental distinctions.

6.4 Carbonate production on the Pedroche platform

The Pedroche Formation contributes to a strengthening picture of carbonate deposition on Cambrian shelves and platforms. Within the Arroyo Pedroche and Pilgrimage Road sections, thrombolite microbialites are both the most conspicuous and most abundant contributors to platform deposition, comprising 55 – 60% of all carbonates (Table 1). Coated grains account for 8 – 13% of carbonate accumulation, while the remaining 31 – 32% encompasses recrystallized carbonate textures, and other, minor lithologies (Table 1). Skeletons, especially archaeocyaths, are locally conspicuous and abundant, but because facies other than archaeocyath rudstone contain such a low skeletal component, the total measurable contribution of carbonate skeletons to the platform accumulation is low, perhaps 5 – 6% by volume. This is not too different from Cambrian samples measured in China, Newfoundland, Labrador and the North American Cordillera, and well below skeletal abundances in most Middle Ordovician and younger deposits (Hicks and Rowland, 2009; Pruss et al, 2010, 2012). That is, despite the fact that Pedroche Formation and coeval carbonates accumulated during the acme of Cambrian body plan diversification (Knoll and Carroll, 1999; Erwin et al., 2011), and despite the observation that most of the skeletal designs evolved by animals appeared during this interval (Thomas et al., 2000), skeletons remained a subsidiary component of carbonate deposits.

Clearly, Pedroche and other Cambrian carbonate accumulations are distinct from younger examples. How do they compare with older platform and shelf deposits? While countless stratigraphic sections transect Proterozoic carbonate platforms, few studies compile the

percentage of lithofacies at the outcrop-scale. Knoll and Swett (1990) reported that stromatolites, oncolites and microbial laminates make up ~25% of all carbonates of the ca. 800–750 Ma Akademikerbreen Group, Spitsbergen, with oolite contributing ~15%, and the remaining ~60% consist of micrite, calcarenite (carbonate grainstone), and rudstone derived from the erosion and re-deposition of mostly micrite lithologies. Thus, even more than this Neoproterozoic succession, microbialites represent a significant component of Pedroche carbonate accumulation.

Proterozoic and Cambrian carbonates differ, of course, in the *nature* of constituent microbialites, being largely stromatolitic in older rocks and thrombolitic in the Cambrian Period (Grotzinger, 1990; Grotzinger et al., 2000). Indeed, in the Pedroche Formation, stromatolites make up only about 0.25% of the sedimentary package as a whole. In modern settings, thrombolites develop in subtidal environments where eukaryotic algae, especially macroscopic algae, colonize microbialite surfaces (Feldmann and McKenzie, 1998; Andres and Reid, 2006). The holdfasts of sessile benthic invertebrates might also disrupt microbial lamination (Grotzinger et al., 2000). Such observations provide a framework for interpreting Pedroche and other Cambrian thrombolites. These structures accreted subtidally, where the influence of traction load sediments was small (e.g., Pratt and James 1982, 1986). Fossils and molecular clocks support the hypothesis that the diversification of green algae and sessile benthic animals contributed to the distinctive fabrics of subtidal Cambrian microbialites (e.g., Grotzinger et al., 2000). In general then, the introduction of animal and algal macrobenthos into early Phanerozoic marine communities modified the morphologies, fabrics, and facies distribution of stromatolites and thrombolites, but did not result in the elimination of microbial build-ups from carbonate platforms and shelves. That occurred later, with the mid-Ordovician radiation of heavily skeletonized sessile macrobenthos.

Increasingly, then, the Cambrian stands out as a transitional interval of carbonate deposition, with carbonate production still linked to the physical and microbial processes that had governed carbonate deposition for billions of years, but with evolving algae and animals beginning to exert a quantifiable influence on the processes, loci and fabrics of shelf and platform carbonates.

7. CONCLUSIONS

Carbonate carbon isotope data from three stratigraphic sections of the Pedroche Formation provide the first chemostratigraphic curve for Cambrian stratigraphy of the Ossa Morena geotectonic zone, Iberia. The Pedroche Formation captures the apex of an ~3‰ positive $\delta^{13}C_{carb}$ excursion preceding a plateau around -1.5‰. Within the context of trilobite, small shelly fossil, and archaeocyath biostratigraphy, we correlate this isotopic variability to excursion IV of the Siberian Atdabanian chemostratigraphic framework, correlative to Cambrian Series 2, Stage 3.

Thrombolites and archaeocyath-bearing inter-reef and flanking-reef talus represent loci for skeletal carbonate production and accumulation within the Pedroche Formation, with skeletal material comprising a maximum of 21.5% of total carbonate. Of the skeletal material quantified, archaeocyaths contributed an average of ~68%, with the remainder attributable to small shelly fossils, trilobites, and calcitic brachiopods. The production and export of skeletal material beyond these depositional environments contributed little to coeval carbonate accumulation. Instead, microbial and abiotic carbonates dominated. Despite an important skeletal presence, carbonate accumulation and distribution within the Cambrian Pedroche Formation appears more similar to Neoproterozoic accumulations than Phanerozoic skeletal reef ecosystems.

REFERENCES

Ábalos, B., Carreras, J., Druguet, E., Escuder Viruete, J., Gómez Pugnaire, M. T., Lorenzo Álvarez, S., Quesada, C., Rodríguez-Fernández, L. R., Gil Ibarguchi, J. I., 2002, Variscan and pre-Variscan Tectonics, in: Gibbons, W., and Moreno., T. (Eds.), The Geology of Spain. Geological Society of London, Bath, U.K., pp. 155-183.

Andres, M.S., Reid, P.R., 2006. Growth morphologies of modern marine stromatolites; a case study from Highborne Cay, Bahamas. Sedimentary Geology 185, 319–328.

Babcock, L.E., Peng, S., 2007. Cambrian chronostratigraphy: Current state and future plans. Palaeogeography, Palaeoclimatology, Palaeoecology 254, 62–66.

Bard, J.P., Burg, J.-P., Matte, Ph., Ribeiro, A., 1980. La Chaîne Hercynienne d'Europe occidentale en termes de tectonique des plaques, in: Cogné, J., Slansky, M. (Eds.), Géologie de l'Europe. Mémoire du Bureau de Recherches Géologiques et Minières 108, 233–246.

Bottjer, D.J., Davidson, E.H., Peterson, K.J., Cameron, R.A., 2006. Paleogenomics of echinoderms. Science 314, 956–960.

Brasier, M.D., Rozanov, A., Yu., Zhuravlev, A. Yu, Corfield, R.M., Derry, L.A., 1994. A carbon isotope reference scale for the Lower Cambrian succession in Siberia: report of IGCP project 303. Geological Magazine 131, 767–783.

Cabanás, R., 1971. Observaciones sobre el Cámbrico de la provincia de Córdoba. Boletín Geológico y Minero 82(3-4), 105-107.

Cabanás, R., Meléndez, B., 1966. Notas estratigráficas de la Provincia de Córdoba. Nota sobre un nuevo fósil del Cambriano. Notas y Comunicaciones del Instituto Geológico y Minero de España 90, 77-84.

Carbonell, A., 1926. Nota sobre los yacimientos de "Archaeocyathidos" de la Sierra de Córdoba y deducción para el análisis tectónico. Boletín del Instituto Geológico y Minero de España, 3ª ser., 4ª part., 47, 311-315.

Carbonell, A., 1929. Un nuevo yacimiento de Archaeocyathidae en Córdoba. Consecuencias tectónicas. Memorias de la Real Sociedad Española de Historia Natural 15(1), 271-274.

Carbonell, A., 1930 a-g. Informe referente a las canteras de caliza de Majanillo y Mirabuenos, desde el punto de vista de la fabricación de cemento. Revista Minera Metalúrgica y de Ingeniería, 3216-3234.

Cowan, C.A., James, N.P., 1993. The interactions of sea-level change, terrigenous sediment influx, and carbonate productivity as controls on Upper Cambrian Grand Cycles of western Newfoundland, Canada. Geological Society of America Bulletin 105, 1576–1590.

Dallmeyer, R.D., Martínez García, E. (eds.), 1990. Pre-Mesozoic Geology of Iberia. Springer, New York.

Debrenne, F., 2007. Lower Cambrian archaeocyathan bioconstructions. Comptes Rendus Palevol 6, 5–19.

Derry, L.A., 2010. A burial diagenesis origin for the Ediacaran Shuram-Wonoka carbon isotope anomaly. Earth and Planetary Science Letters 294, 152–162.

Dornbos, S.Q., Bottjer, D.J., 2000. Evolutionary paleoecology of the earliest echinoderms: Helicoplacoids and the Cambrian substrate revolution. Geology 28, 839–842.

Eguiluz, L., Gil Ibarguchi, J. L., Ábalos, B.,Apraiz, A., 2000. Superposed Hercynian and Cadomian orogenic cycles in the Ossa-Morena Zone and related areas of the Iberian Massif. Geological Society American Bulletin, 112: 1398-1413.

Erwin, D. H., Laflamme, M. Tweedt, S.M., Sperling, E.A., Pisani, D., Peterson. K.J., 2011. The Cambrian conundrum: early divergence and later ecological success in the early history of animals. Science 334, 109–1097.

Fedonkin, M., Liñán, E., Perejón, A., 1983. Icnofósiles de las rocas precámbrico-cámbricas de la Sierra de Córdoba, España. Boletín de la Real Sociedad Española de Historia Natural, Geología 81(1-2), 125-138.

Feldmann, M., McKenzie, J., 1998. Stromatolite-thrombolite associations in a modern environment, Lee Stocking Island, Bahamas. Palaios 13, 201–212.

Fernández-Remolar, D. C., 1996. Los microfósiles problemáticos del Cámbrico Inferior de la Sierra de Córdoba: datos preliminares. Coloquios de Paleontología 48, 161-173.

Fernández-Remolar, D. C., 1998. Estudio paleontológico de taxones problemáticos del Cámbrico de Sierra Morena. Tesis Doctoral. Universidad Complutense de Madrid. Departamento de Paleontología. Madrid, Universidad Complutense de Madrid, pp. 306.

Fernández-Remolar, D.C., 1999. Las calizas fosforíticas del Ovetiense Inferior de la Sierra de Córdoba, España. Boletín de la Real Sociedad Española de Historia Natural (Sección Geológica) 95(1-4), 15-45.

Fernández-Remolar, D. C., 2001. Chancelloridae del Ovetiense Inferior de la Sierra de Córdoba, España. Revista Española de Paleontología 16(1), 39-61.

Fernández-Remolar, D., 2002. First record of Tannuolina Fonin & Smirnova, 1967 (Tomotiida) from the lower cambrian pedroche formation, southern spain. Revista Española de Micropaleontología 34(1), 39-51.

Flügel, E., 2004. Microfacies of carbonate rocks: Analysis, Interpretation, and Application. Springer, New York.

Gozalo, R., Liñán, E., Palacios, T., Gámez-Vintaned, J. A., Mayoral, E., 2003. The Cambrian of the Iberian Peninsula: An overview. Geologica Acta 1(1), 103-112.

Grotzinger, J.P., 1989. Facies and evolution of Precambrian carbonate depositional systems: emergence of the modern platform archetype. Society of Economic Paleontologists and Mineralogists Special Publication 44, 79–106.

Grotzinger, J.P., 1990. Geochemical model for Proterozoic stromatolite decline. American Journal of Science 290A, 80–103.

Grotzinger, J.P., Knoll, A.H., 1999. Stromatolites in Precambrian carbonates: Evolutionary mileposts or environmental dipsticks? Annual Review of Earth and Planetary Sciences 27, 313–358.

Grotzinger, J.P., James, N.P. 2000, Precambrian carbonates: Evolution of understanding. Society for Sedimentary Geology (SEPM) Special Publication 67, 3–22.

Grotzinger, J.P., Watters, W.A., Knoll, A.H., 2000. Calcified metazoans in thrombolite-stromatolite reefs of the terminal Proterozoic Nama Group, Namibia. Paleobiology 26, 334–359.

Gubanov, A.P., Fernández-Remolar, D.C., Peel, J.S., 2004. Early Cambrian molluscs from Sierra de Córdoba (Spain). Geobios 37, 199–215.

Hernández Pacheco, E., 1907. Los martillos de piedra y las piedras con cazoletas de las antiguas minas de cobre de la Sierra de Córdoba. Boletín de la Real Sociedad Española de Historia Natural 7: 279-292.

Hernández Pacheco, E., 1917. La fauna primordial de la Sierra de Córdoba. Asociación Española para el Progreso de las Ciencias. Conferencias. Sección 4ª Ciencias Naturales, 76-85.

Hernández Pacheco, E., 1918a. Les Archaeocyathidae de la Sierra de Córdoba (Espagne). Compte Rendus des séances de l'Academie des Sciences 166, 691-693.

Hernández Pacheco, E., 1918b. Le Cambrien de la Sierra de Córdoba (Espagne). Compte Rendus des séances de l'Academie des Sciences 166, 611-613.

Hernández Pacheco, E., 1926. La Sierra Morena y la llanura Ibérica (Síntesis geológica). XIV Congreso Geológico Internacional, Instituto Geológico y Minero de España.

Hernández-Sampelayo, P., 1933. El Cambriano en España. Memoria XVI Congreso Geológico Internacional, Madrid, Instituto Geológico y Minero de España.

Hernández-Sampelayo, P., 1935. Explicación del nuevo mapa geológico de España: El Sistema Cambriano. Memoria del Instituto Geológico y Minero de España 1, 297-525.

Hicks, M., Rowland, S.M., 2009. Early Cambrian microbial reefs, archaeocyathan inter-reef communities, and associated facies of the Yangtze Platform. Palaeogeography, Palaeoclimatology, Palaeoecology 281, 137–153.

Hinz-Schallreuter, I., Gozalo, R., Liñán, E., 2008. New bradorid arthropods from the Lower Cambrian of Spain. Micropaleontology 53, 497–510.

Holland, S.M., 1995. The stratigraphic distribution of fossils. Paleobiology 21, 92–109.

Ingram, R.L., 1954. Terminology for the thickness of stratification and parting units in sedimentary rocks. Bulletin of the Geological Society of America 65, 937-938.

James, N. P., Debrenne, F., 1980. Lower Cambrian bioherms: pioneer reefs of the phanerozoic. Acta Palaeontologica Polonica 25(3-3), 655-668.

Jensen, S., Palacios, T., Martí Mus, M., 2010. Revised biochronology of the Lower Cambrian on the Central Iberian zone, Iberian massif, Spain. Geological Magazine 147, 690–703.

Julivert, M., Fontboté, J. M., Ribeiro, A., Nabais-Conde, L. E., 1972. Mapa Tectónico de la Península Ibérica y Baleares a escala 1:1,000,000. Memoria explicativa [1974]. IGME, Madrid, 113 pp.

Knauth, L.P., Kennedy, M.J., 2009. The late Precambrian greening of the Earth. Nature 460, 728-732.

Knoll, A.H., Carroll, S.B., 1999. The early evolution of animals: Emerging views from comparative biology and geology. Science 284, 2129–2137.

Knoll, A.H., Swett, K., 1990. Carbonate deposition during the late Proterozoic Era: an example from Spitsbergen. American Journal of Science 290-A, 104–132.

Kouchinsky, A., Bengtson, S., Pavlov, V., Runnegar, B., Torssander, P., Young, E., Ziegler, K., 2007. Carbon isotope stratigraphy of the Precambrian–Cambrian Sukharikha River section, northwestern Siberian platform. Geological Magazine 144, 1–10.

Kouchinsky, A., Bengtson, S., Runnegar, B., Skovsted, C., Steiner, M., Vendrasco M., 2012. Chronology of early Cambrian biomineralization. Geological Magazine 149, 221–251.

Landing, E., Geyer, G., Brasier, M.D., Bowring, S.A., *in press*. Cambrian Evolutionary Radiation: Context, correlation, and chronostratigraphy—overcoming deficiencies of the first appearance datum (FAD) concept. Earth-Science Reviews.

Landing, E., Bowring, S.A., Davidek, K.L., Westrop, S.W., Geyer, G., Heldmaier, W., 1998. Duration of the Early Cambrian: U-Pb ages of volcanic ashes from Avalon and Gondwana. Canadian Journal of Earth Sciences 35, 329–338.

Liñán, E., 1974. Las formaciones cámbricas del norte de Córdoba. Acta Geológica Hispánica 9, 21-26.

Liñán, E., 1978. Bioestratigrafía de la Sierra de Córdoba. Tesis Doctoral, Universidad de Granada, Granada: 212 pgs.

Liñán, E., Dabrio, C., 1974. Litoestratigrafía del tramo inferior de la Formación Pedroche (Cámbrico inferior, Córdoba). Acta Geológica Hispánica 9(1): 21-26.

Liñán, E., Gámez-Vintaned, J. A., 1993. Lower Cambrian paleogeography of the Iberian Peninsula and its relations with some neighbouring European areas. Bulletin de la Societé Géologique France 164(6), 831-842.

Liñán, E., Mergl, M., 1982. Lower Cambrian Brachiopods of Sierra Morena, SW Spain. Boletín de la Real Sociedad Española de Historia Natural, Sección Geológica 80, 207-220.

Liñán, E., Palacios, T., 1983. Aportaciones micropaleontológicas para el conocimiento del límite Precámbrico-Cámbrico en la Sierra de Córdoba, España. Comunicações dos Serviços Geológicos de Portugal 69(2), 227-234.

Liñán, E., Quesada, C., 1990. Rift Phase (Cambrian), in: Dallmeyer, R.D., Martínez García, E. (Eds.), Pre-Mesozoic Geology of Iberia. Springer, New York, pp. 259–266.

Liñán, E., Sdzuy, K., 1978. A trilobite from the Lower Cambrian of Córdoba (Spain) and its stratigraphical significance. Senckenbergiana Lethaea 59(4/5), 387-399.

Liñán, E., Álvaro, J., Gozalo, R., Gámez-Vintáned, J. A., Palacios, T., 1995. El Cámbrico Medio de la Sierra de Córdoba (Ossa-Morena, S de España): trilobites y paleoicnología. Implicaciones bioestratigráficas y paleoambientales. Revista Española de Paleontología 10(2), 219-238.

Liñán, E., Dies, M.E., Gámez Vintaned, J.A., Gozalo, R., Mayoral, E., Muñiz, F., 2005. Lower Ovetian (Lower Cambrian) trilobites and biostratigraphy of the Pedroche Formation (Sierra de Córdoba, southern Spain). Geobios 38, 365–381.

Liñán, E., Gonçalves, F., Gámez Vintaned, J. A., Gozalo, R., 1997. Evolución paleogeográfica del Cámbrico de la Zona de Ossa-Morena basada en el registro fósil, in: Araújo, A. A., Pereira Évora, M. F. (Eds.), Estudo sobre a Geologia da Zona de Ossa-Morena (Maciço Ibérico), Livro de Homenagem a Professor Francisco Gonçalves. Universidade de Évora, 1-26.

Liñán, E., Gozalo, R., Dies Álvarez, M.E., Gámez Vintaned, J.A., Zamora, S., 2008. Nuevos trilobites del Ovetiense inferior (Cámbrico Inferior bajo) de Sierra Morena (España). Ameghiniana 45, 123–128.

Liñán, E., Moreno-Eiris, E., Perejón, A., Schmitt, M., 1981. Fossils from the basals levels of the Pedroche Formation, Lower Cambrian (Sierra Morena, Córdoba, Spain). Boletin de la Real Sociedad Española de Historia Natural, Sección Geológica 79, 277-286.

Liñán, E., Perejón, A., Sdzuy, K., 1993. The Lower-Middle Cambrian stages and stratotypes from the Iberian Peninsula: a revision. Geological Magazine 130, 817–833.

Lotze, F., 1945. Zur Gliederung der Variszidem der Iberischen Meseta. Geotektonische Forschungen 6, 78-92.

Maloof, A.C., Schrag, D.P., Crowley, J.L., Bowring, S.A., 2005. An expanded record of Early Cambrian carbon cycling from the Anti-Altas Margin, Morocco. Canadian Journal of Earth Sciences 42, 2195–2216.

Maloof, A.C., Porter, S.M., Moore, J.L., Dudás, F.Ö., Bowring, S.A., Higgins, J.A., Fike, D.A., Eddy, M.P., 2010a. The earliest Cambrian record of animals and ocean geochemical change. Geological Society of America Bulletin 122, 1731–1774.

Maloof, A.C., Ramezani, J., Bowring, S.A., Fike, D.A., Porter, S.M., Mazouad, M., 2010b. Constraints on early Cambrian carbon cycling from the duration of the Nemakit-Daldynian–Tommotian boundary $\delta^{13}C$ shift, Morocco. Geology 38, 623–626.

Matte, P., 1991. Accretionary history and crustal evolution of the Variscan belt in Western Europe. Tectonophysics 196: 309-337.

Menéndez, S., Moreno-Eiris, E., Perejón, A., 1999. Los arqueociatos y las facies carbonatadas de Cámbrico Inferior del Arroyo Guadalbarbo, Córdoba, España. Boletín de la Real Sociedad de Historia Natural, Sección Geológica 94(3-4), 63-91.

Moreno-Eiris, E., 1987a. Los montículos arrecifales de Algas y Arqueociatos del Cámbrico inferior de Sierra Morena I: Estratigrafía y facies. Boletín Geológico Minero 98(3): 295-317.

Moreno-Eiris, E., 1987b. Los montículos arrecifales de Algas y Arqueociatos del Cámbrico inferior de Sierra Morena II: Las algas calcáreas. Boletín Geológico Minero 98(4): 449-459.

Moreno-Eiris, E., 1987c. Los montículos arrecifales de Algas y Arqueociatos del Cámbrico inferior de Sierra Morena III: Microfacies y Diagénesis. Boletín Geológico Minero 98(5): 591-621.

Moreno-Eiris, E., 1987. Los montículos arrecifales de Algas y Arqueociatos del Cámbrico inferior de Sierra Morena IV: Bioestratigrafía y Sistemática de los Arqueociatos. Boletín Geológico Minero 98(6), 729-779.

Moreno-Eiris, E., Perejón, A., Rodríguez, S., Falces, S., 1995. Paleozoic Cnidaria and Porífera from Sierra Morena. VII International Symposium on Fossil Cnidaria and Porífera, 16-22 September, 1995 Field Trip D. Madrid.

Myrow, P.M., Taylor, J.F., Runkel, A.C., Ripperdan, R.L., 2012. Mixed siliciclastic-carbonate upward-deepening cycles of the upper Cambrian inner detrital belt of Laurentia. Journal of Sedimentary Research 82, 216–231.

Payne, J.L., Lehrmann, D.J., Wei, J., Knoll, A.H., 2006. The pattern and timing of biotic recovery from the end-Permian mass extinction on the Great Bank of Guizhou, Guizhou Province, south China. Palaios 20, 63–85.

Peng, S., Babcock, L.E., 2011. Continuing progress on chronostratigraphic subdivision of the Cambrian System. Bulletin of Geosciences 86, 391–396.

Perejón, A., 1971. Pachecocyathus, nuevo género de Archaeocyathidos del Cámbrico español. Estudios Geológicos 4, 143-149.

Perejón, A., 1975a. Nuevas Faunas de Arqueociatos del Cámbrico Inferior de Sierra Morena (I). Tecniterrae 8, 8-29.

Perejón, A., 1975b. Arqueociatos de los subórdenes Monocyathina y Dokidocyathina. Boletín de la Real Sociedad de Historia Natural, Sección Geológica 73(1-4), 125-145.

Perejón, A., 1975c. Arqueociatos Regulares del Cámbrico Inferior de Sierra Morena (SW de España). Boletín de la Real Sociedad de Historia Natural, Sección Geológica 73(1-4), 147-193.

Perejón, A., 1976a. Nuevas Faunas de Arqueociatos del Cámbrico Inferior de Sierra Morena (II). Tecniterrae 9, 7-24.

Perejón, A., 1976b. Nuevos datos sobre los Arqueociatos de Sierra Morena. Estudios Geológicos 32(1), 5-33.

Perejón, A., 1977. Arqueociatos con túmulos en el Cámbrico Inferior de Córdoba (Sierra Morena Oriental). Estudios Geológicos 33(6), 545-555.

Perejón, A., 1986. Bioestratigrafía de los Arqueociatos en España. Cuadernos de Geología Ibérica 9, 213–216.

Perejón, A., 1989. Arqueociatos del Ovetiense en las sección del Arroyo Pedroche, Sierra de Córdoba, España. Boletín de la Real Sociedad Española de Historia Natural (Geología) 84, 143–247.

Perejón, A., 1994. Palaeogeographic and biostratigraphic distribution of Archaeocyatha in Spain. Courier Forschungsinstitut Senckenberg 172, 341–354.

Perejón, A., Moreno-Eiris, E., 2006. Biostratigraphy and paleobiogeography of the archaeocyaths on the south-western margin of Gondwana. Zeitschrift der deutschen Gesellschaft für Geowissenschaften 157(4), 611-627.

Perejón, A. Moreno-Eiris, E., 2007. Ovetian cryptic archaeocyaths, lower Cambrian from Las Ermitas (Córdoba, Spain). In: Hubmann, B., Piller, W.E., (Eds.), Fossil Corals and Sponges. Proceedings of the 9th International Symposium on Fossil Cnidaria and Porifera. – Österr. Akad. Wiss., Schriftenr. Erdwiss. Komm. 17, 113–137.

Perejón, A., Moreno-Eiris, E., Liñán, E., Sequeiros, L., 1996. The Cambrian of the Sierra de Córdoba. (Ossa- Morena Zone. Sierra Morena), in: Liñán E., Gozalo, R. (Eds.), II Field Conference of the Cambrian stage subdivision working groups. Internacional Subcomission on Cambrian stratigraphy. Spain, 13-21 Sept. 1996. Field Trip Guide and Abstracts, 45-55.

Pérez-Estaún, A., Bea, F., 2004. Macizo Ibérico. in: Vera, J.A. (Ed.), Geología de España, Sociedad Geológica de España e Instituto Geológico de España, 21-230.

Peterson, K.J., Lyons, J.B., Nowak, K.S., Takacs, C.M., Wargo, M.J., McPeek, M.A., 2004. Estimating metazoan divergence times with a molecular clock. Proceedings of the National Academy of Sciences 101, 6536–6541.

Pratt, B.R., 1984. *Epiphyton* and *Renalcis* – Diagenetic microfossils from calcification of coccoid blue-green algae. Journal of Sedimentary Petrology 54, 948–971.

Pratt, B.R., James, N.P., 1982. Cryptalgal-metazoan bioherms of Early Ordovician age in the St-George Group, Western Newfoundland. Sedimentology 29, 543–569.

Pratt, B.R., James, N.P., 1986. The St. George Group (Lower Ordovician) in western Newfoundland: tidal flat island model for carbonate sedimentation in shallow epeiric Seas. Sedimentology 33, 313–343.

Pruss, S.A., Finnegan, S., Fischer, W.W., Knoll, A.H., 2010. Carbonates in skeleton-poor seas: New insights from Cambrian and Ordovician strata of Laurentia. Palaios 25, 73–84.

Pruss, S.A., Clemente, H., 2011. Assessing the role of skeletons in Early Paleozoic carbonate production: Insights from Cambro-Ordovician strata, Western Newfoundland. In: Laflamme, M., Schiffbauer, J.D., Dornbos, S.Q. (Eds.), Quantifying the Evolution of Early Life, Numerical approaches to the evaluation of fossils and ancient ecosystems. Springer, New York, 462 pp.

Pruss, S.A., Clemente, H., Laflamme, M., 2012. Early (Series 2) Cambrian archaeocyathan reefs of southern Labrador as a locus for skeletal carbonate production. Lethaia 45, 401–410.

Quesada, C., 1990, Precambrian sucessions in SW Iberia: their relationship to "Cadomian" orogenic events, in: D'Lemos, D. S., Strachman, R. A., Topley, C. G. (Eds.), The Cadomian Orogeny. Geological Society Special Publication 51: 353-362.

Rodríguez-Martínez, M., Heim, C., Simon, K., Zilla, T., Reitner, J., 2011. *Tolypammina gregaria* Wendt 1969-Frutexites Assemblage and Ferromanganese Crusts: A Coupled Nutrient-Metal Interplay in the Carnian Sedimentary Condensed Record of Hallstatt Facies (Austria), in: Reitner, J., Quéric, N.-V., Arp, G. (Eds.), Advances in Stromatolite Geobiology, Springer, New York.

Rowland, S.M. Gangloff, R.A., 1988. Structure and paleoecology of Lower Cambrian reefs. Palaios 3, 111–135.

Rozanov, A.Yu, Parkhaev, P.Yu., Demidenko, Yu., Skorlotova, N.A., 2011. *Mobergella radiolata*—a possible candidate for defining the base of Cambrian Series 2 and Stage 3. Museum of Northern Arizona Bulletin 67, 304–306.

Sarmiento, J.L. Gruber, N., 2006. Ocean biogeochemical dynamics. Princeton University Press, New Jersey.

Schmitt, M., 1982. Columnar stromatolites from the Lower Cambrian Formation Pedroche, Sierra Morena, S. Spain. Boletín de la Real Sociedad Española de Historia Natural, Sección Geológica 80(1-4), 5-23.

Shapiro, R. S., 2000. A comment on the systematic confusion on thrombolites. Palaios 15, 166-169.

Simon, W., 1939. Archaeocyathea: I. Kritischie Sitchung der Spuer Familie. II. Die Fauna im Kambrim der Sierra Morena (Spanien). Abhandlungen Senckenbergischen Naturforshenden Gessellschaft 448, 1-87.

Smith, A.B., 1985. Cambrian eleutherozoan echinoderms and the early diversification of edrioasteroids. Palaeontology 28, 715–756.

Steiner, M., Li, G., Ergaliev, G., 2011. Toward a subdivision of the traditional Lower Cambrian. Museum of Northern Arizona Bulletin 67, 306–308.

Thomas, R.D.K., Shearman, R.M., Stewart, C.W., 2000. Evolutionary exploitation of design options by the first animals with hard skeletons. Science 288, 1239–1242.

Van der Plas, L., Tobi, A.C., 1965. A chart for judging the reliability of point counting results. American Journal of Science 263, 87–90.

Vennin, E., Álvaro, J.J., Moreno-Eiris, E., Perejón, A., 2003. Early Cambrian coelobiontic communities in tectonically unstable crevices developed in Neoproterozoic andesites, Ossa-Morena, southern Spain. Lethaia 36, 53–65.

Zamarreño, I., 1977. Early Cambrian Algal Carbonates in Southern Spain, in: Flügel, E. (Ed.), Fossil Algae: Recent Results and Developments. Springer-Verlag, Berlín, pp. 360-365.

Zamarreño, I, Debrenne, F., 1977. Sédimentologie et biologie des constructions organogénes du Cambrien inféreur du Sud de l'Espagne. Mémoires du Bureau de Recherches Géologiques et Miniéres 89, 49-61.

Zeebe, R.E., Westbroek, P., 2003. A simple model for the $CaCO_3$ saturation state of the ocean: The "Strangelove", the "Neritan", and the "Cretan" Ocean. Geochemistry, Geophysics, Geosystems 4, 1104, doi:10.1029/2003GC000538.

Zhu, M.Y., Babcock, L.E., Peng, S.C., 2006. Advances in Cambrian stratigraphy and paleontology: integrating correlation techniques, paleobiology, taphonomy and paleoenvironmental reconstruction. Palaeoworld 15, 217–222.

FIGURE 1—Geology and map of the study area. A) Generalized Neoproterozoic to Cambrian stratigraphy of the Ossa Morena Zone, Iberian massif (adapted from Gubanov et al., 2004). B) Google Earth image with locations (white dots) of the three measured stratigraphic sections near the city of Córdoba, Spain.

FIGURE 2—Lithostratigraphy and $\delta^{13}C_{carb}$ chemostratigraphy of the Pedroche Formation. LE = Cerro de Las Ermitas section; PR = Pilgrimage Road section; AP = Arroyo Pedroche section. Samples of lithologies point-counted for percent constituent components are denoted with a small arrow next to the stratigraphic height. PR and AP $\delta^{13}C_{carb}$ chemostratigraphy are plotted as 3-pt running averages. Thrombolite megastructure codes (A-0 through A-V) are described in the text and illustrated in Figure 4.

FIGURE 3—Lithologic character of the thrombolite lithofacies. A) Isolated, bioherm surrounded by bedded carbonate and siliciclastics (AP 49.0). The dashed line delineates the contact between the thrombolite bioherm and onlapping siltstone beds. B) Columnar heads separated by siliciclastic siltstone. The dashed line outlines one columnar thrombolite head from surrounding siltstone. C) Thrombolite biostrome with interbeds and irregular drapes of siltstone. D) Archaeocyath clasts within a thrombolitic bed.

FIGURE 4—Schematic of the lithofacies present in the Pedroche Formation. Facies A: Calcimicrobial thrombolite (see representative photographs in Figs. 3 and 5). See text for descriptions of isolated (A-0), biohermal (A-I, A-II, and A-III), and biostromal (A-IV and A-V) megastructures and the figure inset for a key to the mesoclot textures that comprise the internal mesostructure of thrombolite megastructures (mesostructures a – j). Facies B: Nodular limestone that surrounds calcimicrobial thrombolite bioherms (A-I and A-II) and displays a mottled texture imparted by thrombolitic mesoclots. Facies C: ooid, oncoid, and peloid grainstone within massive lenses (facies C1); small, channelized lithosomes (C2); and planar cross-bedded tabular beds (C3; see representative photographs in Figs. 6 and 7). Facies assemblage D: interbedded massive carbonate mudstone, bioclastic wackestone, and archaeocyathan packstone–floatstone–rudstone, and siliciclastic siltstone (see representative photographs in Figs. 8, 9 and 10). These lithologies grade into and out of one another over a sub-cm spatial scale, thus we do not subdivide this facies into individual lithologic components.

FIGURE 5—Photomicrographs of the modes of biological preservation within the Arroyo Pedroche and Pilgrimage Road sections. (Photomicrographs at 6.3x magnification.) A) Arboreal thrombolite mesoclot texture (AP 49.5 m). B) Epiphyton comprising a thrombolite mesoclot (AP 49.5 m). C) Dolomitized trilobite carapace (width = 6 mm; AP 92.6 m). D) Calcitic brachiopod (AP 92.6 m). E) Smally shelly fossil (AP 61.0 m).

FIGURE 6—Lithologic character of the ooid/oncoid/peloid grainstone lithofacies. A) Fine-grained, well-sorted ooid grainstone (AP 61 m). B) Poorly-sorted ooid/oncoid/peloid grainstone (scale bar = 1 cm).

FIGURE 7—Photomicrographs of the ooid/oncoid/peloid grainstone lithofacies taken at 6.3x magnification. An ooid replaced by dolomite rhombs (oomold) in A) plane-polarized light (AP 92.6 m) and B) cross-polarized light (AP 92.6 m). C) A peloid replaced by ferroan dolomite rhombs (AP 17.0 m). D) An ooid with a micritic cortoid fabric (AP 61.0 m). E) An ooid with a micritic cortoid fabric retaining a faint radial arrangement of neomorphosed crystals (AP 92.6 m). F) A nephroid peloid (AP 17.0 m).

FIGURE 8—Lithologic and petrographic character of the interbedded carbonate mudstone, bioclastic wackestone, archaeocyathan floatstone–packstone–rudstone and siliciclastic siltstone lithofacies (facies assemblage D) of the Cerro de Las Ermitas section. A) Outcrop appearance of this spatially-variable lithofacies (block pictured is located just above the measured stratigraphic section). B) Oriented bioclasts within an archaeocyathan rudstone. Rudstone facies common from LE 33.5 – 50 m. C) Photomicrograph of archaeocyathan boundstone where *Archaeopharetra* (Zones I-III) can be distinguished (scale bar = 4 mm; LE 31.5 m). Photomicrographs of the matrix micro-fabrics D) mcr1, E) mcr2, and F) the late-stage cement sp (as described in the main text; all from sample LE 18.0 m).

FIGURE 9—Photomicrographs of archaeocyath-bearing lithofacies and mode of archaeocyath preservation. A) Thin-section LE 18.0 m with text and arrows labeling relevant textures and features. SSF = small shelly fossil. B) An archaeocyath (*Nochoroicyathus)* with a silty microspar (mcr1) infilling the central cavity and intervallum (LE 48.0 m), a drusy microspar (mcr2) molding the walls, and an oncolitic halo surrounding the skeleton. C) An archaeocyath with mcr1 infilling the central cavity and intervallum and both mcr2 and a coarse spar (sp) molding the intervallum and walls (LE 29.0 m). D) An archaeocyath (family Ajacicyathidae) with mcr2 molding the inner walls and sp infilling the central cavity and intervallum (LE 18.0 m). Scale bars represent 5, 0.5, 2 and 1 mm for frames A-D, respectively.

FIGURE 10—Modes of biological preservation (exclusive of archaeocyaths) within the interbedded carbonate mudstone, bioclastic wackestone, archaeocyathan floatstone–packstone–rudstone and siliciclastic siltstone (lithofacies assemblage D). Photomicrograph (at 6.3x magnification) of A) a SSF from sample LE 18.0 m, B) a SSF from sample LE 33.0 m, and C) an unidentified bioclast from sample LE 48.0 m.

FIGURE 11—The percent skeletal contribution within the Pedroche Formation as determined from point counts of representative petrographic thin-sections (see Table 2 for data). Individual circles represent data from a single thin section. The average value for each column is marked with a horizontal black line. A) Percent skeletal contribution by carbonate lithofacies. Samples

representative of the carbonate mudstone (n = 5), bioclastic wackestone (n = 6), and archaeocyath rud./flts./pkst. (rudstone / floatstone / packstone; n = 5) lithofacies derive exclusively from section LE. Samples representative of thrombolite (n = 5) and oo./on./pel. (ooid/oncoid/peloid) grainstone lithofacies (n = 9) derive from sections AP and PR. B) Taxonomic identity of the skeletal contribution (i.e., archaeocyath versus small shelly fossil (SSF)) to the archaeocyathan rudstone/floatstone/packstone lithofacies and C) the bioclastic wackestone lithofacies.

FIGURE 12—The percent constituent components of the carbonate lithofacies of the Pedroche Formation as determined from point counts of representative petrographic thin-sections (see Table 2 for data). Individual circles represent data from a single thin section. The average value for each column is marked with a horizontal black line. A) Constituent components of the bioclastic wackestone and archaeocyathan packstone–floatstone–rudstone lithofacies (facies assemblage D). B) Constituent components of the thrombolite lithofacies (facies A). C) Constituent components of the ooid/oncoid/peloid grainstone lithofacies (facies C).

FIGURE 13—A comparison of the percent skeletal contribution to archaeocyath-bearing reef and inter-reef lithologies of the Pedroche Formation and other reef/inter-reef localities. Individual circles represent data from a single thin section. The average value for each study is marked with a horizontal black line. A) total skeletal contribution, B) archaeocyath skeletal contribution, and C) non-archaeocyath skeletal contribution to reef and inter-reef lithologies. D) Average proportion of archaeocyath (white) versus non-archaeocyath (black) skeletal material from the Pedroche Formation (this study) and the two other early Cambrian localities discussed.

TABLE 1—The percent contribution of carbonate lithofacies (rows) to the total meterage of measured stratigraphic sections (columns) of the Pedroche Formation. (The carbonate-normalized percent carbonate lithofacies are reported in parentheses.)

TABLE 2—Raw point-count data from representative samples of the Cambrian Series 2, Stage 3 Pedroche Formation, Spain. Samples LE, AP, and PR were collected from the Cerro de Las Ermitas, Arroyo Pedroche, and Pilgrimage road section, respectively. Lithologic classification was determined by petrographic examination. Lithological abbreviations represent: Mdst = mudstone, Wkst = wackestone, Grnst = grainstone, Rud = rudstone, and Th = thrombolite. Constituent component abbreviations represent: A. = archaeocyath, Biocl. = bioclastic, Oo. = ooid, On. = oncoid, and Pel. = peloid. Numerical values in the table represent the abundance of identified components counted within a given thin-section. SSF = small shelly fossil.
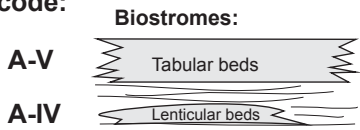
TABLE 3—Average percent of the constituent components (columns) of carbonate lithofacies (rows) of the Pedroche Formation.
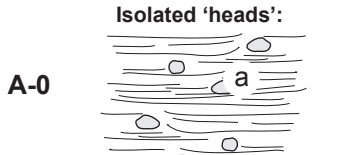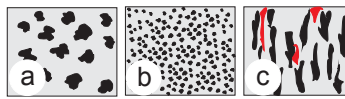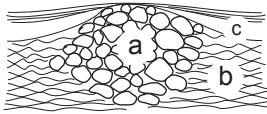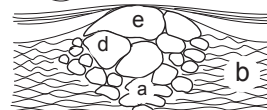
A

Series	Iberian Stage	Formation	
€Series 3 (?)	Bilbilian-Caesaraugustan	Los Villares	
	Bilbilian	Castellar	
€Series 2	Marianian	Santo Domingo	
Ovetian	**Pedroche**	
Terreneuvian	Corduban	Torreárboles	
Neoprot.		San Jerónimo	

B

Pilgrimage Road (PR)

Cerro de Las Ermitas (LE)

Arroyo Pedroche (AP)

CÓRDOBA

Córdoba, Spain

1 km

A — onlapping siltstone / thrombolite bioherm

B

C — thrombolite / siltstone

D — archaeocyath / small mesoclot / 1 cm

Facies code:

Calcimicrobial Thrombolite:

Biostromes:

Internal structure:

Mesostructure:

A-V Tabular beds

j i h

h i j

A-IV Lenticular beds

a e h
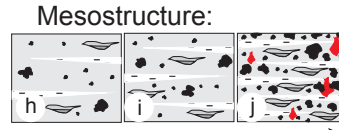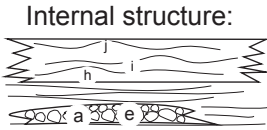
Increase in silt content, the density of clots, and fenestral and irregular cavities.

Bioherms:

A-III

a a

Ex situ blocks

f g

A-II &B

e d a b

a d e

5 cm

A-I & B

a c b

a b c

Isolated 'heads':

A-0 a

Nodular Limestone:

B → b
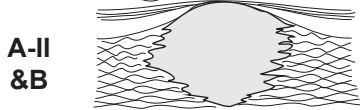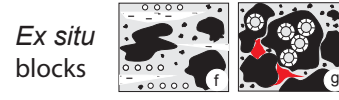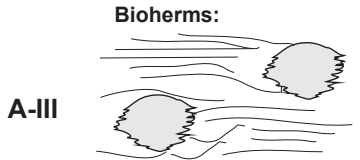
Mesoclots:

⬛ Large, irregular mesoclots (10-15 cm)

Small, irregular mesoclots (10-15 cm)

Columnar/digitate mesoclots (1 cm wide, 3-4 cm long)

Small, rounded mesoclots (< 5 mm diameter)

⬜ Grey, massive matrix

Silt intercalations

Archaeocyath

∘∘∘ Ooids

Oncoids

Peloids

Fenestral cavity

Irregular, red infilling

Ooid/oncoid/peloid grainstone:

C-1

C-2

C-3

Interbedded carbonate mudstone, bioclastic wackestone, archaeocyathan packstone-floatstone-rudstone, and siliciclastic silstone:

Facies D

A

archaeocyathan packstone–
floatstone–rudstone with
carbonate mudstone and
bioclastic wackestone

siliciclastic
siltstone

B

C

D

E

F

A

hematitic overgrowth (frutexites)

vein

SSF

stylolite

hematitic stromatolite

coarse spar (sp)

archaeocyath (imaged in (d))

drusy microspar (mcr2)

silty microspar (mcr1)

B

mcr2

mcr1

oncolitic halo

C

mcr2

mcr1

sp

D

mcr2

sp

A — Skeletal contribution by lithofacies

B — Skeletal identity within the archaeocyathan rudstone/floatstone/packstone facies

C — Skeletal identity within the bioclastic wackestone facies

Bioclastic wackestone and archaeocyathan
floatstone/packstone/rudstone facies

Calcimicrobial thrombolite facies

Ooid/oncoid/peloid grainstone facies

A Total skeletal contribution to inter-reef and reef flank lithologies (facies assemblage D)

% total skeletons

This Study   Pruss et al. (2012)   Hicks and Rowland (2009)

B Archaeocyath skeletal contribution to inter-reef and reef flank lithologies (facies assemblage D)

% archaeocyath skeletons

This Study   Pruss et al. (2012)   Hicks and Rowland (2009)   Rowland and Gangloff (1988)

C Other skeletal contribution to inter-reef and reef flank lithologies (facies assemblage D)

% non-archaeocyath skeletons

This Study   Pruss et al. (2012)   Hicks and Rowland (2009)

D

32% 68%   26% 74%   31% 69%

This Study   Pruss et al. (2012)   Hicks and Rowland (2009)

Table 1

Carbonate Lithofacies	Arroyo Pedroche	Pilgrimage Road	Cerro de Las Ermitas
Calcimicrobial thrombolite (facies A)	27% (60%)	26% (55%)	0%
Ooid/oncoid/peloid grainstone (facies C)	3% (8%)	6% (13%)	0%
Inter-reef / reef-flank facies (facies assemblage D)	0%	0%	100%
Other carbonate	14% (32%)	15% (31%)	0%

Table 2

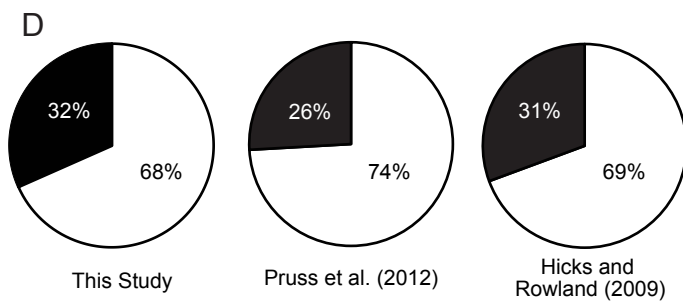| Sample	Lithology	Micrite	Spar	Siliciclastics & Stylocumulate	Vein	Ooid	Peloid	Archaeocyath	Trilobite	SSF	Clotted Micrite & Microbial	Other & Indistinguisable	Total Points
LE 16.5 m	Mdst	192	2	4	0	0	0	0	0	1	0	1	200
LE 18.0	A. Rud./Flts./Pkst.	110	27	11	6	0	0	17	0	11	17	1	200
LE 19.0	Mdst	169	7	3	9	0	0	0	0	1	0	0	189
LE 21.0	Mdst	187	0	8	1	0	0	1	0	3	0	0	200
LE 22.0 m	A. Wkst	75	91	19	0	0	0	10	0	0	0	5	200
LE 29.0 m (1)	Biocl. Wkst / A. Rud	122	6	33	0	0	0	22	0	12	0	3	198
LE 29.0 m (2)	Biocl. Wkst / A. Rud	132	1	32	0	0	0	12	0	4	0	0	181
LE 31.5 m	A. Rud./Flts./Pkst.	108	45	9	1	0	0	27	0	7	0	3	200
LE 32.0 m	A. Rud./Flts./Pkst.	145	8	31	0	0	0	1	0	11	0	4	200
LE 33.0 m	Biocl. Wkst	66	90	1	0	0	0	31	0	10	0	2	200
LE 35.0 m	Biocl. Wkst	153	0	20	2	0	0	1	0	9	0	5	190
LE 36.0 m	Biocl. Wkst / A. Rud	103	17	55	0	0	0	3	0	8	0	2	188
LE 40.0 m	Wkst / Mdst	160	4	11	2	0	0	1	0	6	0	5	189
LE 42.0 m	Mdst	187	9	0	2	0	0	0	0	2	0	0	200
LE 44.0 m	Mdst	152	2	20	0	0	0	0	0	0	0	0	174
LE 48.0 m	Biocl. / A. Wkst	160	23	2	1	0	0	1	0	8	1	2	198
AP 17.0 m	On. /Pel. Grnst	96	6	5	2	0	0	0	0	0	53	35	197
AP 18.0 m	Th	94	5	5	3	0	0	0	0	0	62	31	200
AP 49.0 m	Th	101	0	10	0	0	0	0	0	0	85	4	200
AP 49.5 m	Th	95	2	5	8	0	0	0	0	0	85	5	200
AP 61.0 m	Oo. / Pel. Grnst	65	4	7	9	68	0	0	0	0	28	5	186
AP 62.2 m	Th	115	0	8	0	0	0	0	0	0	69	8	200
AP 65.0 m	Th	88	0	34	1	0	0	0	0	0	61	16	200
AP 92.6 m	Oo. / Biocl. Grnst	87	2	25	0	51	5	0	4	0	5	2	181
PR 5.0 m	Oo. Grnst	62	4	4	2	112	0	0	0	0	0	2	186
PR 14.0 m	Oo. Grnst	115	3	0	1	75	0	0	0	0	0	6	200
PR 28.0 m	Pel. / Oo. Grnst	77	2	0	6	27	72	0	0	0	0	2	186
PR 30.0 m	Pel. / Oo. Grnst	60	48	4	0	20	63	0	0	0	0	5	200
PR 34.4 m	Pel. / Oo. Grnst	110	4	0	3	14	68	0	0	0	0	1	200
PR 77.5 m	Oo. Grnst	67	2	4	0	88	0	0	0	0	0	3	164

Table 3

Carbonate Lithofacies	Average % Skeletal	Average % Micrite	Average % Clotted Micrite / Microbial	Average % Ooids/Oncoids/Peloids
Calcimicrobial thrombolite (facies A)	0.0	50.0	36.2	0.0
Ooid/oncoid/peloid grainstone (facies C)	0.2	47.3	0.0	44.0
Inter-reef / reef-flank facies (facies assemblage D)	7.6	82.1	0.6	0.0